Environ Fluid Mech
DOI 10.1007/s10652-013-9280-9

ORIGINAL ARTICLE

The role of coherent turbulent structures in explaining scalar dissimilarity within the canopy sublayer

Jing Huang · Gabriel Katul · John Albertson

Received: 3 September 2012 / Accepted: 27 March 2013

Abstract Scalar similarity is widely assumed in models and interpretation of micrometeorological measurements. However, in the air space within and just above the canopy (the so-called canopy sublayer, CSL) scalar similarity is generally violated. The scalar dissimilarity has been mainly attributed to differences in the distribution of sources and sinks throughout the canopy. Since large-scale coherent structures in the CSL (e.g. double roller and sweep/ejection) arise from the instabilities generated by the interaction between the mean flow and the canopy, they may encode key dynamical features about the production term responsible for the source–sink dissimilarity of scalars. Therefore, it is reasonable to assume that the geometric attributes of coherent structures are tightly coupled to the onset and the vertical extent of scalar dissimilarity within the CSL. Large-eddy simulation (LES) runs were used to investigate the role of coherent structures in explaining scalar dissimilarity among three scalars (potential air temperature, water vapour and CO_2 concentration) within the CSL under near-neutral conditions for horizontally uniform but vertically varying vegetation leaf area density. It was shown that coherent structures, when identified from the first mode of a novel proper orthogonal decomposition (POD) approach, were able to capture some features of the scalar dissimilarity in the original LES field. This skill was quantified by calculating scalar–scalar correlation coefficients and turbulent Schmidt numbers of the original field and the coherent structures, respectively. However, coherent structures tend to magnify the magnitude of scalar–scalar correlation, particularly in cases where this correlation is already strong. The ability of coherent structures to describe more complex features

J. Huang · J. Albertson
Department of Civil and Environmental Engineering, Duke University, Durham, NC, USA
e-mail: john.albertson@duke.edu

Present Address:
J. Huang (✉)
CSIRO Marine and Atmospheric Research, GPO Box 3023, Canberra, ACT 2601, Australia
e-mail: jing.duke@gmail.com

G. Katul
Nicholas School of the Environment, Duke University, Durham, NC, USA
e-mail: gaby@duke.edu

Published online: 12 April 2013

such as the scalar sweep-ejection cycle was also explored. It was shown that the first mode of the POD does not capture the relative importance of sweeps to ejections in the original LES field. However, the superposition of few secondary coherent structures, derived from higher order POD modes, largely diminish the discrepancies between the original field and the POD expansion.

Keywords Canopy sublayer · Coherent structure · Large-eddy simulation · Proper orthogonal decomposition · Scalar dissimilarity · Turbulence

1 Introduction

Similarity in turbulent transport of mass (e.g. water vapour and CO_2), heat and momentum is widely assumed in models and interpretation of micro-meteorological measurements. For example, virtually all flux footprint models, which describe the functional relationship between the distribution of a source/sink area of a scalar and the flux of this scalar at a measurement point, assume that all scalars behave similarly (see e.g. [28,29,46,75]). Moreover, turbulent Schmidt numbers (Prandtl number in case of temperature) are traditionally assumed to be unity under neutral and stable conditions (see [23, p. 52]), implying the internal mechanism in turbulent scalar transfer is the same as that of turbulent momentum transfer (often, this equality is referred to as Reynolds analogy).

However, in the air space within and just above the vegetation canopy (the so-called canopy sublayer, or the CSL), field experiments suggest that scalar similarity is generally violated. The correlation coefficient between two passive scalars (s_1 and s_2)$r_{s_1 s_2}$ is commonly used as a measure to evaluate the degree to which these two scalars conform to the similarity assumption [3,24,30,31,37,38]. Its value is expected to be ± 1 if the assumption of scalar similarity holds perfectly. Measurements conducted in the CSL do not support scalar similarity, evidenced by significant departures of $r_{q\theta}$ [37,45] and r_{cq} [64,74] from ± 1, where q represents humidity, θ potential air temperature and c CO_2 concentration. Also, the Schmidt/Prandtl number is often found to be as low as 0.5 within the CSL [25,60,61]. De Bruin et al. [12], Cava et al. [10] and Katul et al. [41] reviewed the causes for the dissimilarity between q and θ and concluded that heterogeneity in the sources/sinks of scalars is a common one in addition to the influence of entrainment and non-steadiness of the data analyzed (though the latter two influences cannot be readily disentangled using single point measurements). Williams et al. [76] investigated how variations in surface heterogeneity induced by seasonal changes affect the extent to which the application of Monin–Obukhov similarity theory (MOST) is weakened in the CSL and concluded that senescence exacerbates the violation of MOST applied to the CSL and also degrades correlations between scalars across a wide range of eddy sizes due to production of heterogeneity in scalar sources/sinks. Recent works have studied the effects of thermal stability on momentum-scalar dissimilarity and concluded the strength of correlation between momentum and scalar fluxes decreases with departures from neutral conditions, which is attributed to the change in the topology of the coherent structures [14,47]. Moreover, the different roles the scalars play in the transport process may contribute to the resulting scalar dissimilarity as well. This may be caused by the active role of θ or various physical processes the scalars are involved in. For example, Scanlon and Kustas [63] studied high-frequency eddy covariance data collected in a maize field and partitioned water vapour and CO_2 fluxes into components related to stomatal processes and non-stomatal processes using scalar dissimilarity.

Large-scale coherent structures have been shown to contribute to the majority of the scalar and momentum fluxes across the canopy–atmosphere interface [19,20,22,34,39,73], thereby potentially encoding significant information about the production term in the scalar–scalar source–sink dissimilarity. Our hypothesis is that their geometric attributes and their degree of coupling to the source–sink scalar distribution within the canopy can explain the onset and degree of this dissimilarity. If these coherent structures are commensurate in size to the length scale over which the scalar–scalar source–sink dissimilarity is occuring, then they are likely to imprint any scalar–scalar source dissimilarity originating from within the canopy onto micro-meteorological measurements in the CSL. If the scalar–scalar source dissimilarity is occuring on length scales much smaller than those characterizing these coherent structures, then this dissimilarity is likely to be 'wiped-out' by the efficient mixing of coherent structures. Lastly, if the scalar–scalar source dissimilarity is occuring on length scales much larger than those characterizing these coherent structures, then the coherent structures will only 'band-pass' the contributions of scalar source dissimilarity existing on length scale commensurate to those of the coherent structures. The major obstacle to testing this hypothesis is that both—the scalar source strength and the penetration of eddies into the canopy vary, in a non-linear manner, with leaf area density (and index). Hence, to test this hypothesis, a large-eddy simulation (LES) model is used with carbon, water and heat exchange included along with all key canopy biophysical considerations to estimate scalar sources and sinks inside the canopy volume. The proper orthogonal decomposition (POD) technique is conducted to quantitatively educe the 3D coherent structures following the approach of [33–35]. The role of these coherent structures in explaining scalar dissimilarity is then examined with a focus on the following research questions: (1) To what extent is the dissimilarity in the source–sink profiles of the scalars reflected in the geometric attributes of the coherent structures? (2) To what extent is the dissimilarity of turbulent Schmidt numbers from unity potentially explained in terms of the degree of organization of coherent structures? (3) To what extent do the coherent structures describe other major characteristics connected with the sweep-ejection cycle in the scalar and momentum transport?

2 Methodology

2.1 Large-eddy simulation

The LES technique is now widely used for investigating high-Reynolds-number turbulent flows in a variety of settings [1,2,4,32–34,44,51,52,56,57,65,72]. In the LES approach, the turbulent motions are resolved from the largest production range down to the scale of the numerical mesh by a space-time integration of a filtered form of the Navier–Stokes equations while the contribution of the subgrid scale (SGS) motions to the resolved ones are approximated. Unlike the traditional Reynolds-averaged models [39,59,77], where all turbulent quantities are averaged out and represented in total with a closure model, the LES technique simulates the dominant flow instabilities and formation of 3D turbulent eddies, thereby supporting a richer analysis of the dynamics of turbulent transport.

Shaw and Schumann [66] introduced the LES technique into the study of canopy turbulence and, since then, its use in investigating the CSL has rapidly expanded [8,13,15,16,34,78,79]. Albertson et al. [4] made the first effort to include the coupled carbon, water and heat exchange at the leaf scale in the LES for 3D canopy flows with dynamic leaf temperature and stomatal aperture. They studied the relative importance of local and global controls of vegetation structures on local scalar concentrations and fluxes and found that the concentrations and velocities exhibit non-local controls while the fluxes do not. A modified version of the code described in [4] is employed here. The horizontal boundary conditions are periodic, and stress-free, zero-flux and no penetration conditions are imposed at the top of the computation domain. The flow is driven by a constant pressure gradient in the streamwise direction. For a detailed description of the equations of the dynamics, the SGS model and numerical schemes, see [4] and references therein.

Here, the simulations were performed on a numeric mesh with $256 \times 128 \times 56$ nodes over a domain of $500 \times 250 \times 500\,\mathrm{m}^3$ (streamwise–spanwise–vertical, or x–y–z, respectively) that covers the lower portion of the ABL. And consequently, the effects of boundary-layer scale eddies are not simulated. The nodes are uniformly spaced in the horizontal plane offering a horizontal resolution of $\Delta x = \Delta y \approx 2.0\,\mathrm{m}$. A 20 m tall vegetation canopy has been simulated as a distributed drag field (described below) that covers the entire horizontal plane homogeneously. Inside the canopy, the nodes are uniformly spaced in the vertical direction with a constant inter-node space of 1 m and, from the canopy top up to the top of the ABL, the grid is vertically stretched using a hyperbolic tangent expansion. The aerodynamic roughness length of the soil surface is set as $z_0 = 0.1$ m, which is generally not important for dense canopies since the majority of the momentum is absorbed by the upper portion of the canopy. The Coriolis force is not included in this study since turbulent flows in the CSL are generally insensitive to the Earth's rotation [34,36,66], particularly when there is a prescribed pressure gradient in the streamwise direction.

In these simulations, the measured vertical distribution of the leaf area of the Duke Forest [17] was used, which is quantified by a local leaf area density $b(x, y, z)$ (LAD, area of plant surface per unit volume). An integration of $b(x, y, z)$ over the vertical range of the canopy results in the leaf area index (LAI), given by,

$$LAI(x, y) = \int_0^h b(x, y, z)\mathrm{d}z, \tag{1}$$

where h is the geometric canopy height. The dimensionless LAD (normalized by LAI and h) is shown in Fig. 1, which is characterized by a primary peak around $z/h = 0.6$ due to the crown of the pine canopy and a secondary peak around $z/h = 0.45$ due to the presence of a hardwood understory. The drag force term is modelled as linear in LAD and quadratic with velocity,

$$F_i = -C_d b \bar{u} u_i, \tag{2}$$

where $\bar{u} = \sqrt{u_i u_i}$ is the modulus of the wind speed, u_i is the resolved velocity component (i.e. the SGS part is excluded) in the x_i direction ($x_1 = x, x_2 = y, x_3 = z, u_1 = u, u_2 = v$ and $u_3 = w$) and C_d is an empirical drag coefficient taken here as 0.13 [11]. To elucidate the effects of vegetation density on scalar transport, three LES experiments with $LAI = 1$, 5 and 9 have been performed, respectively. For all the three LAI cases, the simulated CSL is under slightly unstable to near-neutral stability conditions such that temperature can be generally considered as a passive scalar. More details about the stability conditions will be given in Sect. 3.1.

A detailed description of the scalar exchanges between the leaf surface and its surrounding air is presented in [4] and references therein and will not be repeated here. However, for completeness, the key equations are introduced. The sensible heat exchange between the vegetation and ambient air (h_v) is calculated as

$$h_v = b g_h (\theta_1 - \theta), \tag{3}$$

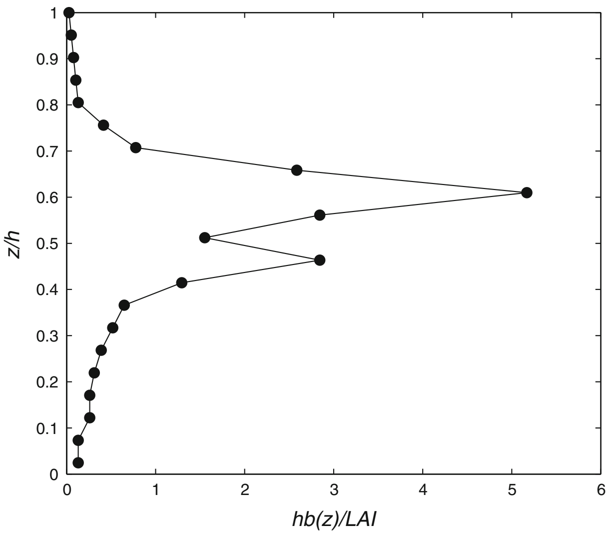

Fig. 1 The normalized canopy leaf area density as a function of normalized height. The normalizing variables are canopy height (h) for vertical dimensions and LAI (LAI)

where g_h is a conductance to heat transfer across the laminar boundary layer on a leaf [7] that varies with the local fluctuating velocity, θ_1 is the temperature of the leaf surface and θ is the temperature of ambient air. The local net rate of carbon uptake (η) depends on biochemical demand of the leaf and the diffusion from ambient air to the chloroplast, where the photosynthetic reactions are either restrained by the amount of absorbed photosynthetically active radiation (PAR) or by the enzyme kinetics of the ribulose biphosphate carboxylase-oxygenase (Rubisco) [18],

$$\eta = \min(A_{par}, A_{ru})b, \tag{4}$$

where A_{par} represents the PAR limited rate and A_{ru} the Rubisco limited rate. The water vapour source term is derived from considerations of the carbon assimilation processes as,

$$e_v = (g_e m_a \rho_a^{-1})(q^*(\theta_1) - q_s)b, \tag{5}$$

where g_e is the stomatal conductance for water vapour (transpiration), which is approximately 1.56 times greater than that for CO_2 [7], m_a is the molecular weight of air, ρ_a is the density of air, $q^*(\theta_1)$ is the saturated specific humidity at the leaf temperature and q_s is the specific humidity of the air at the leaf surface.

Each of the three LAI cases is evaluated under a single mid-day period with high sun angle and a net all-wave radiation of $R_n = 500\,\mathrm{W\,m^{-2}}$ above the canopy. R_n and the PAR, which is a major constraint for the local carbon assimilation rate, are distributed vertically through the canopy volume using a simple one-dimensional radiative algorithm that approximates the binomial probability of radiation interception by the Poisson distribution [4,7]. R_n affects θ_1 through the local vegetation energy balance at each computational node

$$\frac{\partial \theta_1}{\partial t} = \frac{1}{\rho_1 c_p (b\mathrm{d}z)}(R_n - h_v - L_v e_v), \tag{6}$$

where ρ_1 is the mass of foliage per unit leaf area, c_p is the specific heat capacity of the foliage , L_v is the latent heat of vaporisation and dz is the vertical inter-node space. The latent heat flux f_E and the sensible heat flux f_H at the soil surface are estimated with the Priestley–Taylor formulation under the assumption of saturated soil moisture:

$$f_E = \frac{\bar{\Delta}\alpha(R_n^s - f_G)}{\bar{\Delta} + \gamma}, \tag{7}$$

$$f_H = R_n^s - f_G - f_E, \tag{8}$$

where R_n^s is the net radiation at the soil surface, f_G is the soil heat flux modelled here as $f_G = 0.15R_n^s$ [71], $\alpha(= 1.26)$ is the Priestley–Taylor coefficient, γ $(= 0.67\,\mathrm{mbar\,^\circ C^{-1}})$ is the psychrometric constant and $\bar{\Delta}$ $(\mathrm{mbar\,^\circ C^{-1}})$ is the slope of the saturation vapour pressure–temperature curve [7]. Following this brief introduction to the LES, we consider next the detection technique of the coherent structures used, i.e., the POD technique.

2.2 Proper orthogonal decomposition

As earlier mentioned, the POD technique is used to educe the 3D coherent structures. Originally, it was introduced to the study of turbulence by [48–50]. In comparison with other detection techniques of coherent structures, such as conditional sampling and wavelet transform, one merit of the POD lies in its physical interpretation of coherent structures. Specifically, coherent structure shapes identified by the POD optimally and objectively capture the ensemble-averaged variance of turbulent quantities, the turbulent kinetic energy (TKE) in the case of velocity components, while the criteria of the others are more or less arbitrary. In a recent work, Finnigan et al. [20] applied the POD and conditional averaging to the LES data of canopy turbulence. It was found that the coherent structure educed by the POD presents similar geometric features as that obtained by the traditional conditional averaging method with the triggering criterion for the coherent structure selected in a particular manner. The POD technique is outlined here for completeness, while comprehensive reviews can be found elsewhere [5,27,67–69].

We consider three possible state vectors: one containing only the velocity components, ${}^1\mathbf{V} = [u', v', w']$ and the second one is an augmented vector that includes the scalars of interest (and hence is partially sensitive to the coupling between the scalar source strength and the flow), ${}^2\mathbf{V} = [\tilde{u}', \tilde{v}', \tilde{w}', \tilde{c}', \tilde{q}', \tilde{\theta}']$ where $\tilde{u}_i' = u_i'/u_a$, $u_a = \sqrt{\int_H \langle u_i' u_i' \rangle \mathrm{d}z/(3H)}$, and for each scalar (e.g. s), $\tilde{s}_i' = s'/s_a$ and H is the vertical region of interest. This scaling strategy for ${}^2\mathbf{V}$ forces the velocity components to contribute equally as the scalar components to the target of optimization in the POD, i.e., $\int_H \langle \tilde{u}_i' \tilde{u}_i' \rangle \mathrm{d}z = \int_H \langle \tilde{c}'^2 + \tilde{q}'^2 + \tilde{\theta}'^2 \rangle \mathrm{d}z$. The third one contains only the three normalized scalars, i.e., ${}^3\mathbf{V} = [\tilde{c}', \tilde{q}', \tilde{\theta}']$. Due to the homogeneity of our simulation domain in x and y, a direct POD analysis in the physical space produces a series of Fourier modes, which are clearly not in accordance with the localization property of the coherent structures [19,27,33–35,53]. Thus, the POD analysis is conducted in the wavenumber space, which is formulated by the following eigenvalue problem:

$$\int_H \Phi_{ij}(k_x, k_y, z, \tilde{z})\hat{\phi}_j(k_x, k_y, \tilde{z})\mathrm{d}\tilde{z} = \lambda(k_x, k_y)\hat{\phi}_i(k_x, k_y, z), \tag{9}$$

where Φ_{ij} is the spectral-density tensor defined as

$$\Phi_{ij}(k_x, k_y, z, \tilde{z}) = \langle \hat{\mathrm{V}}_i(k_x, k_y, z, t)\hat{\mathrm{V}}_j^*(k_x, k_y, \tilde{z}, t)\rangle_t, \tag{10}$$

where $\langle\rangle_t$ implies the operation of temporal averaging, * represents the complex conjugate, V_i is the ith component of $\mathbf{V}$ and $\hat{\mathrm{V}}_i$ is the forward Fourier transform of V_i, given by

$$\hat{\mathrm{V}}_i(k_x, k_y, z, t) = \iint \mathrm{V}_i(x, y, z, t)e^{-ik_x x - ik_y y}\mathrm{d}x\mathrm{d}y. \tag{11}$$

Through solving Eq. (9) and imposing other physical assumptions (see the detailed approach and equations in Appendix 1), a series of eigenmodes $\psi_i^{(n)}$ (see Appendix 1 for its definition) can be identified from the ensemble of the state vector, which optimally contribute to the overall variance of the state vector in an integral sense. Denoting E as the overall variance and $\Lambda^{(n)}$ as the contribution of the nth eigenmode, we get

$$E = \int_H \langle \mathrm{V}_i \mathrm{V}_i \rangle(z)\mathrm{d}z = \sum_{n=1}^{\infty} \Lambda^{(n)}. \tag{12}$$

The 3D coherent structure has been referred to here as the first eigenmode $\psi_i^{(1)}$ since $\Lambda^{(1)}$ represents the greatest percentage of E out of all other non-Fourier-mode choices of the coherent structure [19,27,33,34,53]. And it is natural to use $\Lambda^{(1)}/E$ to measure the importance of the coherent structures in canopy turbulence. Furthermore, Katul et al. [42] studied the budget equation of the two-scalar covariance $\langle s_1' s_2' \rangle$ and showed that $\langle s_1' s_2' \rangle$ is mainly determined by the TKE and the profile of scalar sources/sinks (see Eq. (8) in [42]). Since the coherent structure optimally captures the variances (TKE for ${}^1\mathbf{V}$ and the sum of TKE and scalar variances for ${}^2\mathbf{V}$), we are in a sound state to utilize the coherent structure to explain the onset and the extent of scalar dissimilarity. Finally, since the enhancement of scalar variances beyond their background state arises from the source/sink activities, it is expected that the addition of scalar variances to the optimization target of the POD relates the coherent structure to the scalar sources/sinks and the extent to which the results (such as $\Lambda^{(1)}/E$ and the geometric features) respectively obtained from the approach of ${}^1\mathbf{V}$ and that of ${}^2\mathbf{V}$ vary can reveal the strength of their interaction.

3 Results and discussion

In this section, the simulation results of three cases with varying LAI values are presented and the effects of the coherent structure on scalar–scalar dissimilarity and scalar-momentum transport dissimilarity are discussed. The basic flow (velocity) statistics are examined so as to assess the general validity of the LES runs vis-à-vis well known properties of CSL turbulence. Then, the profiles of source/sink strength and other basic scalar statistics are shown along with the effects of increasing vegetation density on them. The dissimilarities across scalars and scalar/momentum fluxes are then analyzed quantitatively using global measures including scalar–scalar correlations and turbulent Schmidt numbers as well as local measures such as the role of the sweep-ejection cycle on scalar and momentum transfers, respectively. Furthermore, the geometry of the 3D coherent structure incorporating both velocity components and scalars is revealed and the dissimilarity in the geometric features of different scalars in the coherent structure is then connected to scalar dissimilarity exhibited in the original flow field. The contribution of the coherent structure to scalar dissimilarity is quantified by comparing the results of scalar–scalar correlation, turbulent Schmidt numbers and the relative importance of sweeps to ejections (see Sect. 3.2 for more details) for the coherent structure and the original field, respectively.

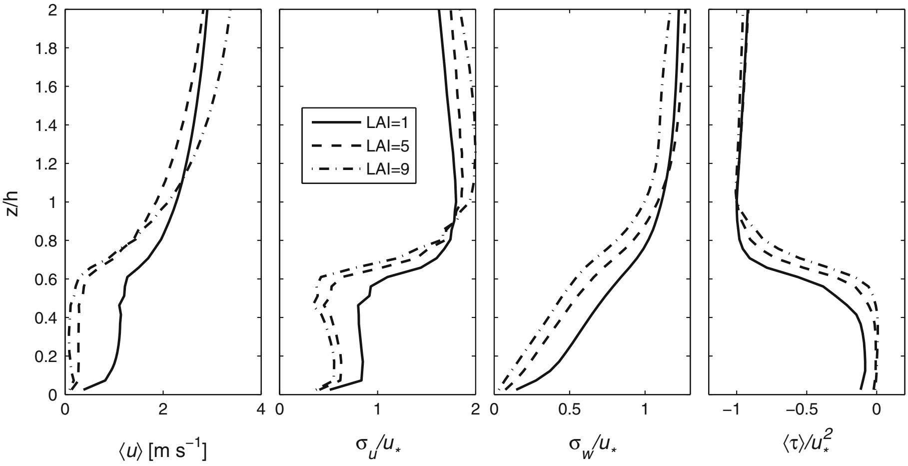

Fig. 2 Vertical profiles of temporal and horizontal mean streamwise velocity $\langle u\rangle$, normalized standard deviation of mean streamwise velocity σ_u/u_*, normalized standard deviation of vertical velocity σ_w/u_* and normalized stress $\langle\tau\rangle/u_*^2$ (from *left to right*)

3.1 Basic flow and scalar statistics

To establish the general validity of the LES experiments, the basic flow velocity statistics at their equilibrium state for $LAI = 1$, 5 and 9 are presented in Fig. 2, including the temporal and horizontal mean streamwise velocity $\langle u\rangle$, the normalized u standard deviation σ_u/u_*, the normalized w standard deviation σ_w/u_*, and the normalized total stress $\langle\tau\rangle/u_*^2$, where τ represents the sum of the resolved stress and the SGS stress and $u_* = \sqrt{-\langle\tau\rangle_{z=h}} = 0.52$, 0.55 and 0.60 m s^{-1} for $LAI = 1$, 5 and 9, respectively. As expected, an increase in LAI results in a decreased $\langle u\rangle$ in the lower canopy; however, above the canopy, there is a tendency of increasing wind speed with increasing LAI, which is due to a 'skimming effect' [4]. The values of σ_u/u_* and σ_w/u_* (e.g. σ_u/u_* is around 2 and σ_w/u_* is around 1 at the canopy top) are consistent with previous results obtained from numerical and wind-tunnel [6] experiments. The small irregularities around $z/h = 0.6$ in the profiles of $\langle u\rangle$ and σ_u/u_* are attributed to the primary peak in the vertical canopy structure shown in Fig. 1 (cf. [34]). Furthermore, Fig. 2 also illustrates major differences in how the canopy attenuates the profiles of σ_u/u_* and σ_w/u_*. The LES results are suggestive that deep inside the canopy, there is significant σ_u/u_*(due to turbulence originating well above the canopy), while σ_w/u_* is significantly attenuated, consistent with a number of field experiments [40,55]. These results are also suggestive that the TKE remains significant inside the canopy even for the largest LAI due to eddies produced above the CSL though these eddies do not contribute much to vertical velocity fluctuations.

In Fig. 3, the normalized vertical profiles of the mean scalar $(\langle s\rangle - s_0)/s_*$, the scalar sources and sinks $\langle S_s\rangle h/u_*/s_*$, the scalar flux $\tau_s/u_*/s_*$ and the scalar variance $\langle s'^2\rangle/s_*^2$ are presented, where $s_0 = \langle s\rangle_{z=h}$, τ_s is the total vertical flux (i.e. the sum of the resolved flux $\langle w's'\rangle$ and the SGS flux) and $s_* = \tau_s^{z=h}/u_*$ for $s = c, q, \theta$ and $LAI = 1$, 5 and 9. Here, $c_* = -0.55$, -1.61 and -1.72 ppm, $q_* = 0.26$, 0.24 and 0.22 g kg^{-1}, $\theta_* = 0.09$, 0.12 and 0.11 K, for $LAI = 1$, 5 and 9, respectively. The general agreement in the mean concentration profiles and the source–sink profiles of CO_2 across the three cases of varying vegetation density reflects the approximate linear relationship between the local net CO_2 uptake rate

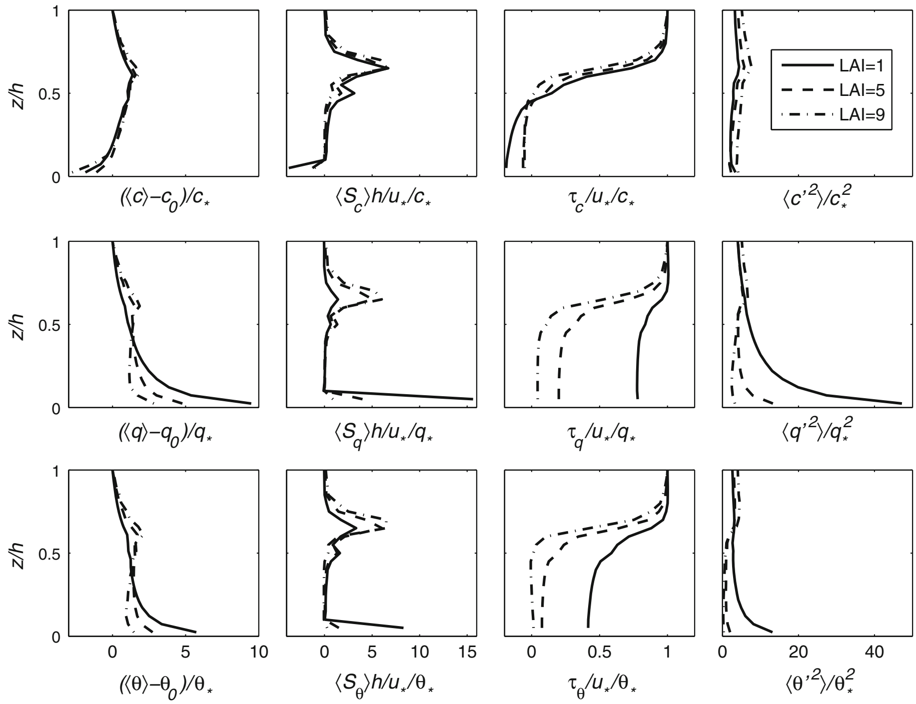

Fig. 3 Vertical profiles of normalized mean scalar, scalar source/sink, vertical flux (including both resolved and SGS fluxes) and variance for CO_2 concentration c (*top row*), water vapour concentration q (*middle row*) and air temperature θ (*bottom row*), respectively. Note that c_* is negative such that $\langle c\rangle - c_0$ and $\langle S_c\rangle$ are of opposite sign to the actual quantities

and the local LAD. However, there is also a minor difference among the source–sink profiles of different LAI values in the sense that the strength increases with LAI above the primary peak of LAD but decreases with LAI below. This vertical pattern is due to the dependence of the local net CO_2 uptake rate on the photosynthetically active radiation availability, which becomes more vertically inhomogeneous as LAI increases with a higher fraction intercepted in the upper canopy layers and less in the sub-canopy [4]. A horizontally homogeneous CO_2 source strength of 2 μmol m^{-2} s^{-1} was assigned at the ground to account for the soil and forest floor respiration. However, the relative importance of this CO_2 source to the integrated CO_2 flux decreases with increasing LAI, as shown in the near-ground portion of the source–sink profile and the flux profile.

The major difference of the source–sink profiles between c, q, θ is that the canopy and the soil sources/sinks are of opposite signs for c (canopy as a sink and soil as a source) but of identical signs for q and θ (both as sources). As expected, the vegetation density has significant effects on the source profiles of the latent and sensible heat fluxes. The source strength at the soil–atmosphere interface decreases while the source strength inside the canopy increases with increasing LAI as a result of canopy radiation interception. The ground becomes the dominant source for the latent and sensible heat fluxes for $LAI = 1$, while the canopy layers dominate for $LAI = 5$ and 9. Consequently, as the canopy becomes denser, the normalized variance generally increases for c inside the canopy and decreases for q and θ from the ground up to around the primary peak of LAD. For any given LAI, the ground is relatively more important (than the canopy) as a source of the latent heat flux than of

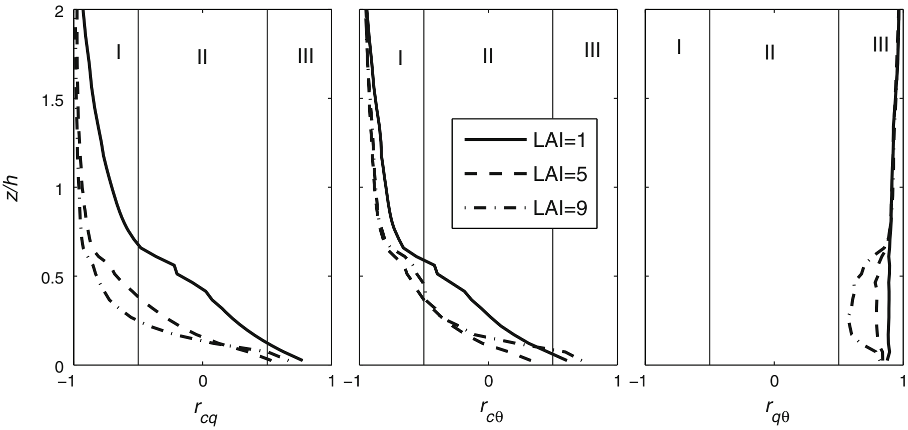

Fig. 4 Vertical profiles of correlation coefficients r_{cq}, $r_{c\theta}$ and $r_{q\theta}$ (from left to right). I, II, III represent the three regions in accordance with the value of correlation coefficients, respectively

the sensible heat flux: the ratio of the strength between the ground source strength and that at the primary peak of LAD for $LAI = 1$ is 11.0 for the latent heat flux but only 2.5 for the sensible heat flux. An examination of the τ_θ profile reveals the CSL is mildly unstable for the three LAI cases. To quantify the stability, we have calculated the flux Richardson number as $R_f = \frac{g}{\langle\theta\rangle}\langle\tau_\theta\rangle/(\langle\tau\rangle\frac{\mathrm{d}\langle u\rangle}{\mathrm{d}z})$, where g is the gravitational acceleration. It turns out that R_f generally falls in the range of [−0.09, −0.02] in the CSL for the three cases except in the near-surface region where the denominator of R_f is close to zero. At the canopy top R_f is approximately −0.08, −0.06, −0.03 for $LAI = 1$, 5 and 9, respectively. This implies that even for $LAI = 1$ the thermal stability is weak within the CSL and for all practical purposes, temperature is approximately a passive scalar here. The normalized variance of CO_2 concentration generally increases with higher vegetation density inside the canopy. Given the sensitivity of the individual scalar variances to LAI variations and given how different these normalized variances are for various scalars and LAI values, the addition of scalar variance in the POD analysis is expected to provide novel information about the coupling between the flow and the vegetation beyond what can be achieved by TKE alone, which is predominantly controlled by σ_u/u_*, and hence eddies not locally originating within the canopy volume.

With these apparent differences in the scalar source/sink and scalar variance profiles, and with the variability occurring on a length scale and position overlapping with canopy coherent structures, one might expect scalar dissimilarity to arise as earlier discussed in the budgets of $\langle s_1' s_2'\rangle$.

3.2 Scalar dissimilarity in the original flow field

One measure often used to quantify scalar similarity between two scalars (s_1 and s_2) is their correlation coefficient $r_{s_1 s_2}$, which is defined as $\langle s_1' s_2'\rangle/\sqrt{\langle s_1'^2\rangle}/\sqrt{\langle s_2'^2\rangle}$ and has an expected value of ±1 for strictly similar scalars. Figure 4 shows the profiles of r_{cq}, $r_{c\theta}$ and $r_{q\theta}$ for the three LAI cases. We split the vertical range of the CSL (i.e. $z/h \subset [0, 2]$) into three regions in accordance with the ranges of the value of $r_{s_1 s_2}$, i.e., region I for $-1 \le r_{s_1 s_2} < -0.5$, region II for $-0.5 \le r_{s_1 s_2} < 0.5$ and region III for $0.5 \le r_{s_1 s_2} \le 1$. Both r_{cq} and $r_{c\theta}$ cover all the three regions. It is clear that the formation of region I is mainly due to the role of the canopy

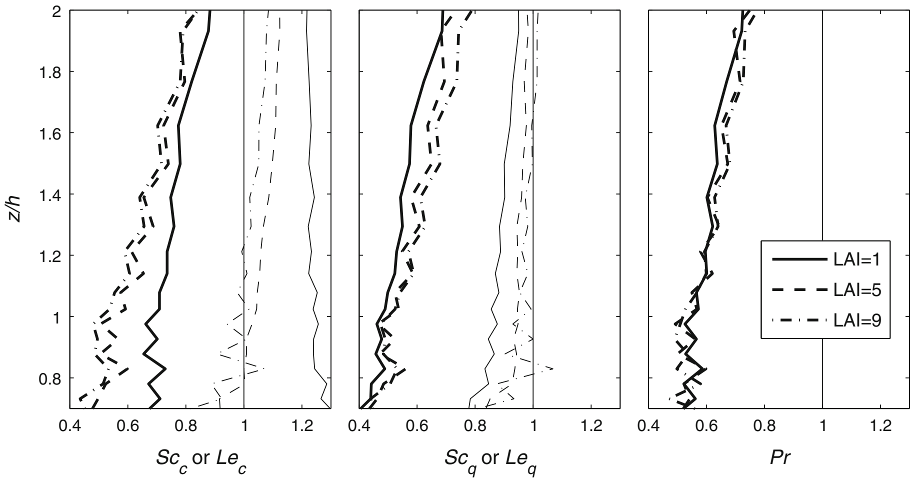

Fig. 5 Vertical profiles of turbulent Schmidt number (or Prandtl number for θ, the *thick lines*) and turbulent Lewis number (the *thin lines*) for c, q and θ (from *left to right*). The *vertical line* of $Sc/Le/Pr = 1$ is also plotted for reference

acting as a sink of CO_2 but a source of water vapour and sensible heat flux. For $c-q$ and $c-\theta$ there is a shallow zone of region III near the soil surface, arising because of the soil being a source of all three scalars. The combined effects of the canopy and the soil act to degrade the modulus of r_{cq} and $r_{c\theta}$, leading to scalar dissimilarity inside the canopy between region I and region III. Region I of r_{cq} extends deeper into the canopy for the denser cases because the processes of transpiration and photosynthesis inside the canopy are regulated by the stomata, which couples the carbon sink and the water vapour source profiles in the canopy. In fact, if the inter-cellular to ambient CO_2 concentration was approximately constant throughout the canopy depth, stomatal regulation of both scalars would be almost identical. For such a case, the water use efficiency becomes almost a constant analogous to a constant Bowen ratio for latent and sensible heat fluxes throughout the canopy layers. However, the biochemical processes controlling photosynthesis, and their switch from temperature to light limitations leads to some CO_2 regulation above and beyond stomatal regulation. Although $r_{q\theta}$ is in region III for the entire CSL under all three LAI cases, the strength of the similarity decreases with increasing LAI approximately below the primary peak of LAD with $r_{q\theta} \approx 0.9$ for $LAI = 1$ and $r_{q\theta} \approx 0.6$ at $z/h \approx 0.2$ for $LAI = 9$. This reduction in $r_{q\theta}$ for the high LAI case is expected given that the sources of water vapour and heat from the soil surface are relatively weak. In addition, the strong correlation in the upper part of the CSL revealed in Fig. 4 is consistent with Fig. 3 in [47] and Fig. 11 in [14] for near-neutral conditions.

In Fig. 5, we present the vertical profiles of the turbulent Schmidt number Sc (Prandtl number Pr for temperature) and the turbulent Lewis number $Le(= Sc/Pr)$ for each LAI and scalar, where $Sc = K_m/K_s$ and K_m and K_s are the turbulent diffusivities for momentum and scalar, respectively. The total momentum and scalar transport (i.e. the sum of the resolved and SGS fluxes) are used to calculate the profiles. They are only shown in the vertical range of $z/h \subset [0.7, 2]$ because below $z/h = 0.7$ Sc and Le exhibit large perturbations due to the vanishingly small amplitude of turbulent diffusivities. Sc generally ranges from 0.4 to 0.9 and Le ranges from 0.8 to 1.3, which are consistent with the values reported in the literature [21,43]. There is a clear dependence of Sc on height for all three scalars, which agrees with the conclusion drawn from the wind tunnel experiment in [43] and are probably

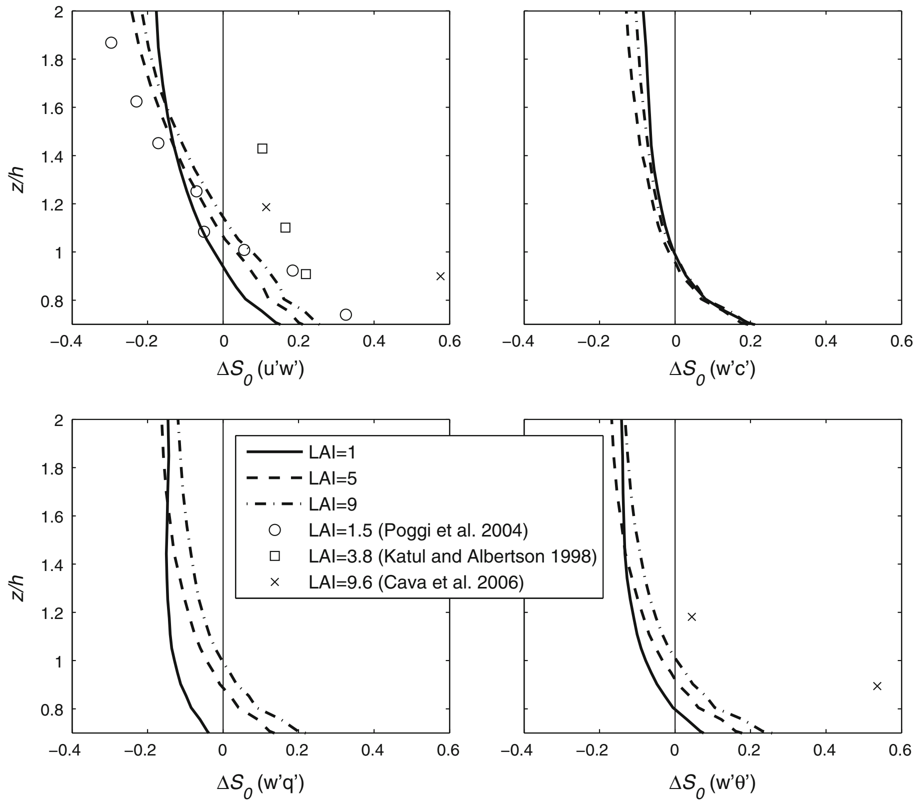

Fig. 6 Vertical profiles of ΔS_0 for momentum and scalar fluxes. Note that for momentum and $w'c'$, ΔS_0 is calculated as the difference between Quadrant IV and Quadrant II; however, for $w'q'$ and $w'\theta'$ it is between Quadrant III and Quadrant I.

caused by coherent structure transporting scalars in a more local manner than the momentum [43]. Likewise, these values are consistent with [25], who reported Sc values as low as 0.5 for a number of forest stands. As Le excludes the effects of momentum transfer, its values are generally closer to unity and are much less height-dependent than Sc, which imply that the transport efficiencies are more similar among scalars than momentum. The dissimilarity in the source–sink profile has a significant impact on Sc as evidenced by Sc_c being greater than Sc_q for the case of $LAI = 1$ but of similar magnitude for the case of $LAI = 9$, and it is similar for Le. This is in accordance with the previous recognition by [59] that the turbulent diffusivity are strongly influenced by the source/sink distribution of the scalar under consideration, and can be understood in the context of Fig. 3: note for $LAI = 1$ the relatively strong ground source causes Sc_q to differ greatly from Sc_c. Since the relative importance of the contribution of the ground surface decreases in the source–sink profile of carbon and water with increasing LAI, Sc_c and Sc_q tend to converge to one another with increasing LAI. Finally, as the effects of LAI on the source/sink profile are less significant for θ than for q (cf. the scalar source/sink profiles in Fig. 3), Pr appears less sensitive to LAI while maintaining a similar trend as Sc_q above the canopy top.

Figure 6 presents an analysis of the sweep-ejection cycle using ΔS_0 to measure the relative importance of sweeps to ejections across the vertical range $z/h \subset [0.7, 2]$. Here, ΔS_0 is defined following [58]:

$$\Delta S_0 = \frac{\langle w's' \rangle_{\text{sweeps}} - \langle w's' \rangle_{\text{ejections}}}{\langle w's' \rangle}. \tag{13}$$

The sweeps and ejections of $\langle w's' \rangle$ are determined using standard quadrant analysis classification. Four quadrants are identified through the combination of the signs of s' (abscissa) and w' (ordinate). Although ΔS_0 is originally defined for stress, these definitions of sweep and ejection can be extended to scalar transport such that the sign of the flux contribution of the sweep and ejection quadrants is consistent with the sign of the total flux. For positive local fluxes (e.g. latent heat flux and sensible heat flux in the entire CSL and CO_2 flux near the ground) the sweeps are in quadrant III and ejections in quadrant I. For negative local fluxes, the sweeps are in quadrant IV and ejections in quadrant II (e.g. CO_2 flux in upper canopy and above and stress), which are consistent with the traditional definitions of sweep and ejection for the turbulent stress. This analysis was performed using only the resolved w and scalar concentrations, which is reasonable because the resolved momentum and scalar fluxes generally capture over 98 % of their corresponding total fluxes in the designated range. The results of ΔS_0 are shown in comparison with previous findings from a flume experiment [55], field experiments in a pine forest [39] and in a mixed coniferous forest [9]. The ΔS_0 for momentum is in a good agreement with the flume result while being generally smaller than the field experiments. As vegetation density increases, sweeps tend to be more important than ejections for $z/h < 1.2$, which was shown to reflect the elevation of the coherent structure due to a better analogy of the CSL with the plane mixing layer [34] and is also consistent with the recent field study by [14]. In fact, these LES results are consistent with the scaling analysis in [54], where ΔS_0 is expressed as:

$$\Delta S_0 = -\frac{\lambda_1}{2\sqrt{2\pi}} \frac{Q}{\langle u'w' \rangle} \left(\frac{1}{\sigma_u} \frac{\partial \sigma_u^2}{\partial z} - \frac{2}{\sigma_w} \frac{\partial \langle u'w' \rangle}{\partial z} \right), \tag{14}$$

where $Q = \sqrt{\langle u_i' u_i' \rangle}$ is the square root of the TKE and λ_1 is a length scale. Because $\partial \sigma_u^2/\partial z \geq 0$ for $z/h < 1.2$ and $\partial \langle u'w' \rangle/\partial z \approx C_d b \langle u \rangle^2$, increasing $C_d b$ (or the inverse of the adjustment length scale) leads to a ΔS_0 that becomes 'elevated' with height with sweeps becoming the dominant mode of momentum transport (i.e. ΔS_0 becoming progressively negative) as evidenced by the profiles in Fig. 2.

The ΔS_0 crosses zero lower for q and θ than for momentum and CO_2, particularly for low LAI cases. This suggests that for sparse canopies, ejections are more important near the canopy top for the vertical transport of q and θ than that of momentum and CO_2, and is probably caused by the role of the ground surface emitting both water vapour and heat, which are transferred to around and above the canopy top by coherent eddies with diameters of approximately one half of the canopy height [62]. This portion of air flow then reinforces ejection motions of latent heat flux and sensible heat flux. Since the relative importance of the source/sink at the ground level decreases with increasing LAI, ΔS_0 tends to increase for q and θ with increasing LAI. For momentum, flume experiments on a sparse rod canopy also demonstrated that ejections dominate near the canopy top when compared to sweeps.

3.3 Scalar dissimilarity in the coherent structure

We now proceed to explore the connection between coherent structures and observed dissimilarity among scalars. First, we show the overall importance of the coherent structures in capturing the resolved TKE and scalar variances as well as momentum and scalar fluxes.

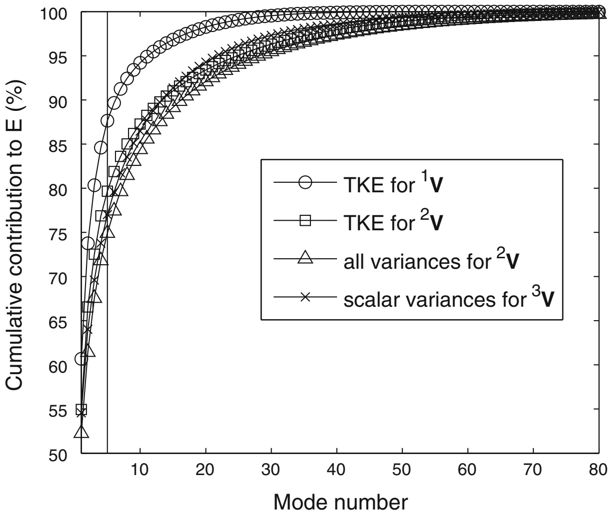

Fig. 7 Cumulative contribution to the integrated sum of variance of the POD modes for three cases: in the first case ${}^1\mathbf{V}$ only three velocity components are incorporated while both velocity components and three scalars are included in the second case ${}^2\mathbf{V}$. The third case ${}^3\mathbf{V}$ contains only the scalars. The *vertical line* indicates the results for five modes. The case of $LAI = 5$ is used to produce all the results

Then, we describe the geometric attributes of these coherent structures using velocity components and flux contribution. Finally, the scalar dissimilarity originating from dissimilarity in sources and sinks encoded by the coherent structure is quantitatively compared with that in the original field through the use of scalar–scalar correlations, turbulent Schmidt numbers and the ability of the coherent structure in reproducing the sweep-ejection cycle.

Figure 7 shows the cumulative contribution to E [i.e. $\sum_{n=1}^{p} \Lambda^{(n)}/E$, see Eq. (25)] of the eigenmodes. Note that TKE converges faster in ${}^1\mathbf{V}$ than in ${}^2\mathbf{V}$ because the structures educed on ${}^2\mathbf{V}$ are optimal in the sense of both velocity components and scalars, thereby degrading the optimization of TKE (in isolation). However, the coherent structures (i.e. the first eigenmode) obtained through ${}^2\mathbf{V}$ still describes approximately 55 % of the total TKE, only 5 % less than the optimum value obtained through ${}^1\mathbf{V}$. Overall, the coherent structure describes approximately 52 % of the sum of all the integrated variances, which equally represent the TKE and scalar variances. Scalar variances in ${}^3\mathbf{V}$ converge slower than TKE in ${}^1\mathbf{V}$ with the leading mode capturing 55 % of the total scalar variances, suggesting that the coherency in terms of scalars in the coherent structure is weaker than in velocity components. The convergence rate for all variances in ${}^2\mathbf{V}$ is close, although slightly lower, to scalar variances in ${}^3\mathbf{V}$, indicating that the leading modes in terms of velocities in ${}^1\mathbf{V}$ are linked to those in terms of scalars in ${}^3\mathbf{V}$.

In addition to the contribution to the variances, we investigate the percentage contribution of the coherent structures to the overall vertical fluxes of momentum and scalars (i.e. the covariance) $p_{\mathrm{V}_i\mathrm{V}_j}$ in Fig. 8, where $p_{\mathrm{V}_i\mathrm{V}_j}$ is defined as,

$$p_{\mathrm{V}_i\mathrm{V}_j} = \frac{\langle \mathrm{V}_i^{(1)}\mathrm{V}_j^{(1)} \rangle}{\langle \mathrm{V}_i\mathrm{V}_j \rangle}, \tag{15}$$

where $\mathrm{V}_i^{(1)}$ is the reconstructed field described by the coherent structures [cf. Eq. (26) and Eq. (27)]. Note that Eq. (15) does not count the SGS fluxes. $p_{w'c'}^{(1)}$ for $LAI = 1$ is noticeably

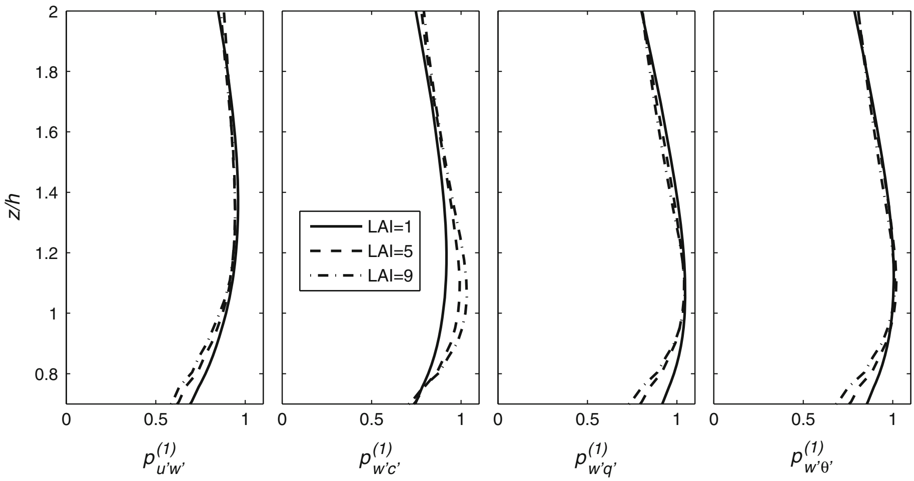

Fig. 8 Vertical profiles of the fraction of the contribution of the coherent structure to the total flux of $u'w'$, $w'c'$, $w'q'$ and $w'\theta'$ (from *left to right*)

smaller than those of other scalars in the range of $z/h \subset [1, 1.4]$, which reflects that the ground CO_2 source offsets the canopy CO_2 sink, and consequently, reduces $w'c'$ in the upper CSL (cf. the profile of τ_c in Fig. 3). The percentage of the contribution of the coherent structure generally ranges from around 60 to over 100, much larger than that for the variances. This is because the incoherent components of the turbulent series can be uncorrelated, thus contributing only a very small amount to the covariances. However, these components still contribute a significant portion to the variance irrespective of the lack of inter-variable correlation (e.g. σ_u^2). The percentage contribution can be over 100 because the variance-oriented optimization of the POD procedure does not capture the covariance in a monotonic way. Other modes could have small contributions of opposite sign. The percentage for the three scalar fluxes generally peaks at or just above the canopy top, indicating the region where the contribution of the coherent structure to the vertical scalar transport is most dominant. However, $p_{u'w'}$ peaks noticeably higher (at $z/h \approx 1.3$) than the scalar fluxes.

Given $p_{\mathrm{V}_i\mathrm{V}_j}$, it is convenient to calculate turbulent Schmidt numbers associated with the coherent structure $Sc_s^{(1)}$, by which we imply a situation where the bulk momentum and scalar transport is approximated by the contribution of the coherent structure while assuming identical mean fields of velocity and scalars. It follows that $Sc_s^{(1)}$ can be expressed by,

$$Sc_s^{(1)} = Sc_s \left(\frac{p_{u'w'}}{p_{w's'}} \right). \tag{16}$$

Figure 9 shows the results of $Sc_s^{(1)}$.$Sc_s^{(1)}$ is similar to Sc_s in the sense that: (1) $Sc_s^{(1)}$ generally increases with height and approaches 1; (2) $Sc_c^{(1)}$ tends to decrease with increasing LAI; (3) $Sc_q^{(1)}$ tends to increase with increasing LAI. The scatter plots contrasting $Sc_s^{(1)}$ and Sc_s reveal that the deviation of $Sc_s^{(1)}$ from Sc_s is generally within the range of $[-0.1, 0.1]$, suggesting the coherent structure has preserved the momentum-scalar transport dissimilarity from the original fields. Note that $Sc_s^{(1)}$ tends to underestimate Sc_s at low values and to overestimate Sc_s at high values with the critical point around 0.7 for all three scalar types and three LAI cases.

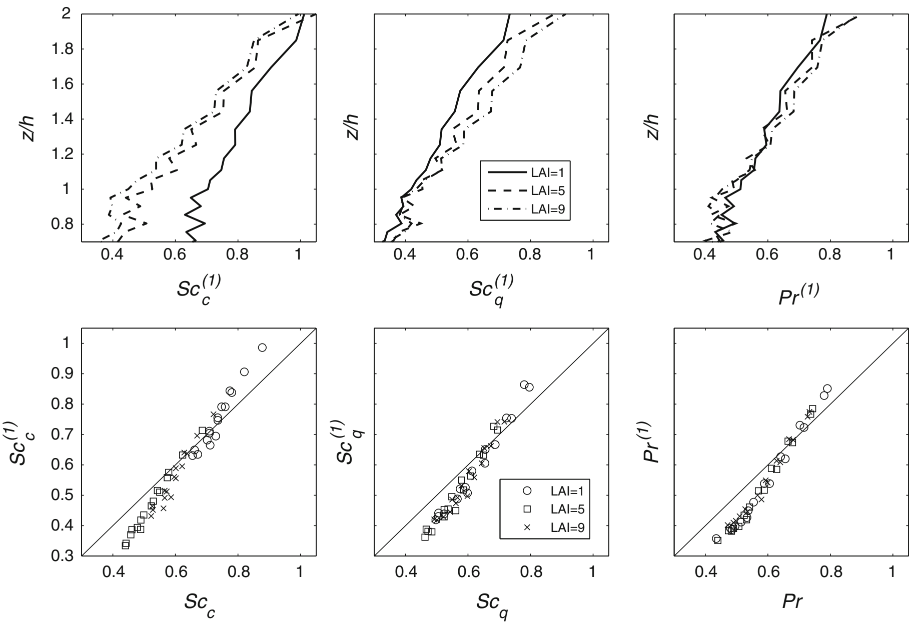

Fig. 9 (*Top row*) Vertical profiles of turbulent Schmidt numbers associated with the coherent structures for c, q and θ (from left to right); (*bottom row*) scatter plots of turbulent Schmidt numbers associated with the coherent structure and from the original for c, q and θ (from *left to right*)

The morphological features of the 3D coherent structure $V_i^{(1)}(r_x, r_y, z)$ are explored and their effects on scalar dissimilarity are discussed first. The central cross-sections of the coherent structure (i.e. $r_x = 0$ and $r_y = 0$) are projected onto the y–z plane and the x–z plane, respectively. The velocity vector plots are presented for $LAI = 5$ whereby the results for the cases of ${}^1\mathbf{V}$ and ${}^2\mathbf{V}$ are contrasted for the projection onto the x–z plane in Fig. 10 and the projection onto the y–z plane in Fig. 11, respectively. In the x–z plane, the coherent structure is characterized by a range of sweep motions centered around the canopy top and $r_x/h = 0$, and a spanwise vortex in the subcanopy region. In the y–z plane, the coherent structure is composed of sweeps framed by a pair of counter-rotating streamwise vortices. These results are also consistent with previous descriptions of the coherent structures conducted in a wind-tunnel [19] and numerical [34] experiments. Note that Finnigan et al. [20] showed that the sweep is typically closely followed by an ejection downstream within the CSL using conditional averaging. However, within the POD framework, the information concerning the sense of rotation of the coherent structures and how they are spatially aligned are carried by the coefficients [i.e. β in Eq. (30)] such that this feature is not readily captured in Figs. 10 and 11. The difference of the results of the coherent structure identified using ${}^1\mathbf{V}$ and ${}^2\mathbf{V}$ appears as that the coherent structure from ${}^1\mathbf{V}$ is generally more compact (spatially). In conjunction with the results shown in Fig. 7, this suggests that there is a strong interaction between the coherent structure and the scalar sources/sinks. By strong interaction, we mean that the size of the coherent structure and the length scale over which the scalar sources/sinks vertically vary are comparable and the coherent structures do not 'average-out' this vertical variation.

Figures 12 and 13 show the comparison between momentum and scalar transport contributions of the coherent structure in the x–z plane at $r_y = 0$ and in the y–z plane at $r_x = 0$, respectively. Both similarity and dissimilarity between momentum and scalar trans-

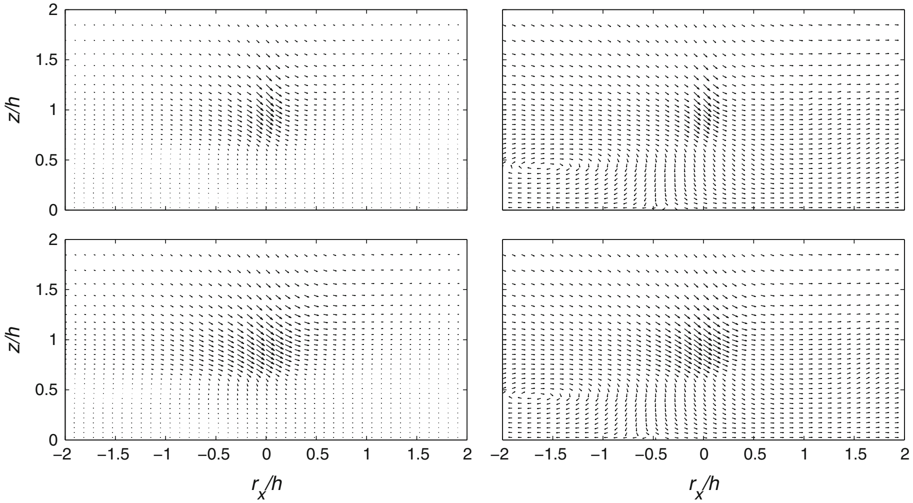

Fig. 10 Quiver plots of the cross-section of the coherent structure on the x–z plane at $r_y = 0$ for $LAI = 5$. The results of the *top row* are obtained from $^1\mathbf{V}$ and the *bottom row* from $^2\mathbf{V}$. In the *panels on the right side*, *arrow* lengths are ununiformly magnified from their corresponding *left panels* in order to reveal flow directions clearly

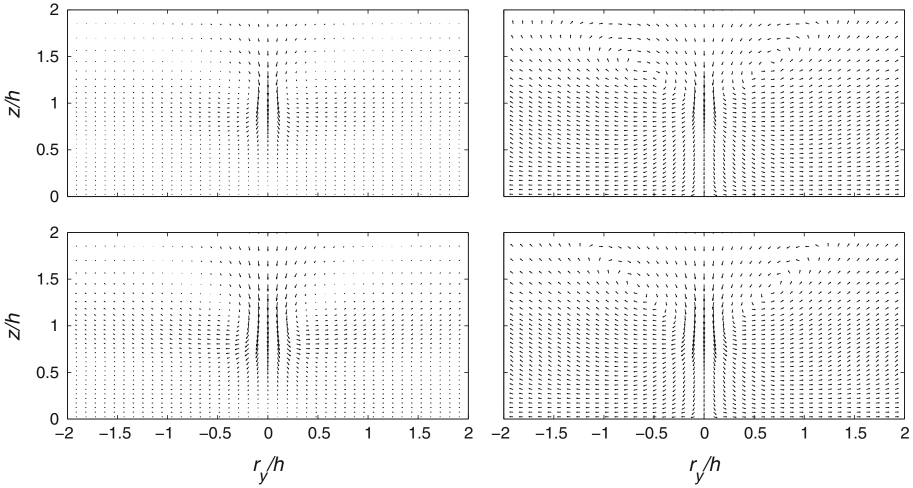

Fig. 11 Quiver plots of the cross-section of the coherent structure on the y–z plane at $r_x = 0$ for $LAI = 5$. The results of the *top row* are obtained from $^1\mathbf{V}$ and the *bottom row* from $^2\mathbf{V}$. In the *panels on the right side*, *arrow* lengths are not uniformly magnified from their corresponding *left panels* to reveal flow directions clearly

port emerge from this comparison. The similarity mainly appears as the core area of the coherent structure (represented by the two cross-sections). The most significant portion of the momentum as well as scalar transport by the coherent structures occurs within the vertical range $z/h \subset [0.6, 1.5]$, which is the central area where the primary instabilities generated by the interaction between the mean flow and the canopy structure arise. As sweep motions arrive at the canopy, they carry air relatively enriched in CO_2 and depleted in water vapour

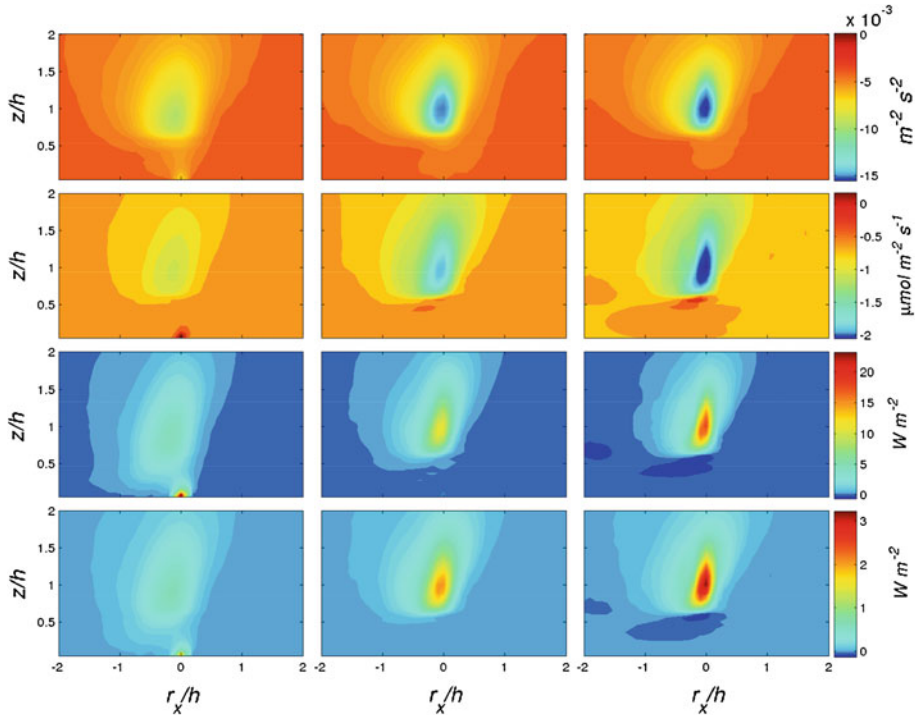

Fig. 12 *Colour plots* of flux contribution of the coherent structures on the x–z plane at $r_y = 0$. Fluxes of momentum, c, q, θ from *top to bottom*, and $LAI = 1, 5, 9$ from *left to right*

from above the canopy to this range. And, as ejection motions are generated from the canopy, they carry air relatively depleted in CO_2 and enriched in water vapour from inside the canopy to this range. The momentum and scalar transport carried by the coherent structures increase with increasing LAI. At $LAI = 1$, the coherent structures do capture the major characteristics of the source–sink profiles of the scalars shown in Fig. 3. The dissimilarity between scalar and momentum transport mainly includes: (1) The role of the soil surface is much more important in the CO_2 source–sink profile for $LAI = 1$ than for $LAI = 5$ and 9 and this source is captured by the large-scale coherent structures. For momentum transport, the aerodynamic roughness length of the soil surface can be important only for $LAI = 1$, which is also captured by the coherent structures. (2) As LAI increases, the relative importance of the soil surface in acting as the source of carbon, water and sensible heat and the sink of momentum decreases, thereby increasing the similarity of scalar transport, as evidenced by the approximation of Sc_c, Sc_q and Pr at $LAI = 9$ in Fig. 5. Another contributor to the scalar transport similarity in dense canopies is the occurrence of the counter-gradient fluxes of carbon, water and sensible heat right below $z/h \approx 0.6$ (the height of the primary peak of the canopy structure profile), which can be explained by sweep motions carrying the air at the level with densest leaf areas that is enriched in water vapour and heat but depleted in CO_2, to the level below as they penetrate through the entire canopy. However, this counter-gradient flux does not exist for momentum because there is negligible momentum flux below $z/h \approx 0.6$ for $LAI = 5$ and $LAI = 9$ (see Fig. 2) despite the presence of a mean velocity gradient. Finally, it is interesting to note that the scale of the coherent structure in x is

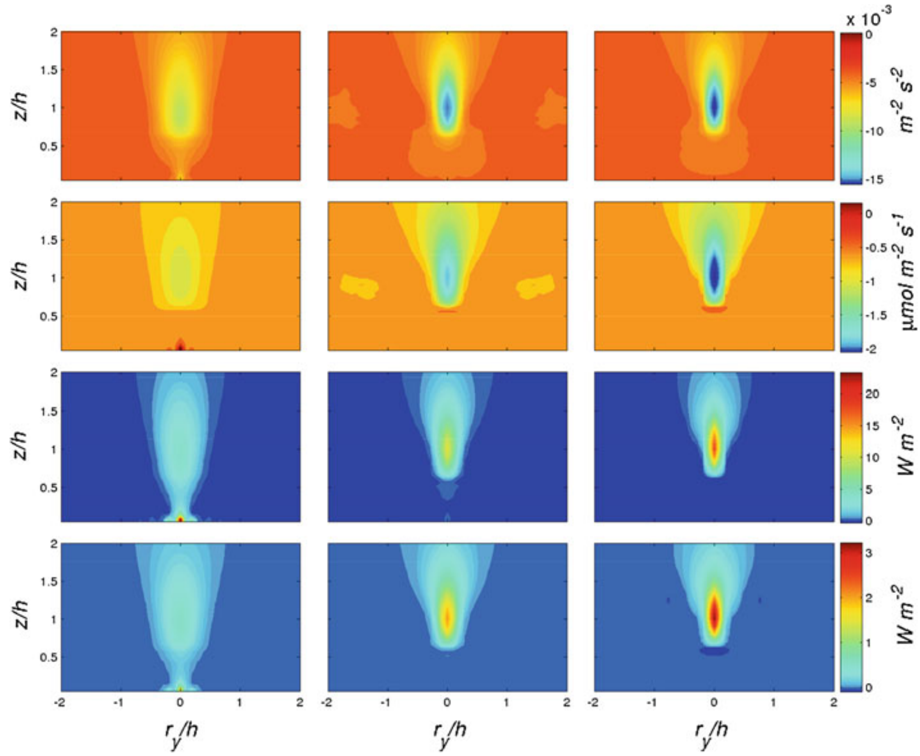

Fig. 13 *Colour plots* of flux contribution of the coherent structures on the y–z plane at $r_x = 0$. Fluxes of momentum, c, q, θ from *top to bottom*, and $LAI = 1, 5, 9$ from *left to right*

about twice of that in y with the significant portion residing in $r_x/h \subset [-1.5, 0.5]$ and $r_y/h \subset [-0.5, 0.5]$.

In addition to revealing the signature of the source–sink dissimilarity carried by the coherent structure with respect to its geometric attributes, we also examine this signature quantitatively through the study of correlation coefficients. Figure 14 shows the correlation coefficients between the scalar components of the coherent structures (represented by $r^{(1)}_{s_1 s_2}$) and the original field $r_{s_1 s_2}$. It is shown that $r^{(1)}_{s_1 s_2}$ retains the basic pattern of $r_{s_1 s_2}$: $r^{(1)}_{cq}$ and $r^{(1)}_{c\theta}$ approach -1 in the upper part of canopy and above, approach 1 close the soil surface and cross zero in between; $r^{(1)}_{q\theta}$ is close to 1 in the entire CSL with slightly lower values in the sub-canopy region. However, unlike $r_{s_1 s_2}$, $r^{(1)}_{s_1 s_2}$ is relatively insensitive to LAI. This can be explained by the fact that in the three LAI cases, the coherent structures all arise from the same Kelvin–Helmholtz instability generated by the vertically inflected mean velocity profile (see[61]). This explanation is supported by the conclusion in [34] that the mixing-layer analogy is well recovered for canopy turbulence with LAI being around and greater than 1. The results of the correlation coefficients for the coherent structures identify region II defined in Sect. 3.2 roughly within the same range of $z/h \subset [0.1, 0.4]$ for $r^{(1)}_{cq}$ and $r^{(1)}_{c\theta}$. The sigmoidal shape of $r_{s_1 s_2} - r^{(1)}_{s_1 s_2}$ suggests that the coherent structure tends to amplify the strength of correlation of the scalar quantities in the original field, particularly when this correlation in the original field is already high. This reinforces the inference in explaining

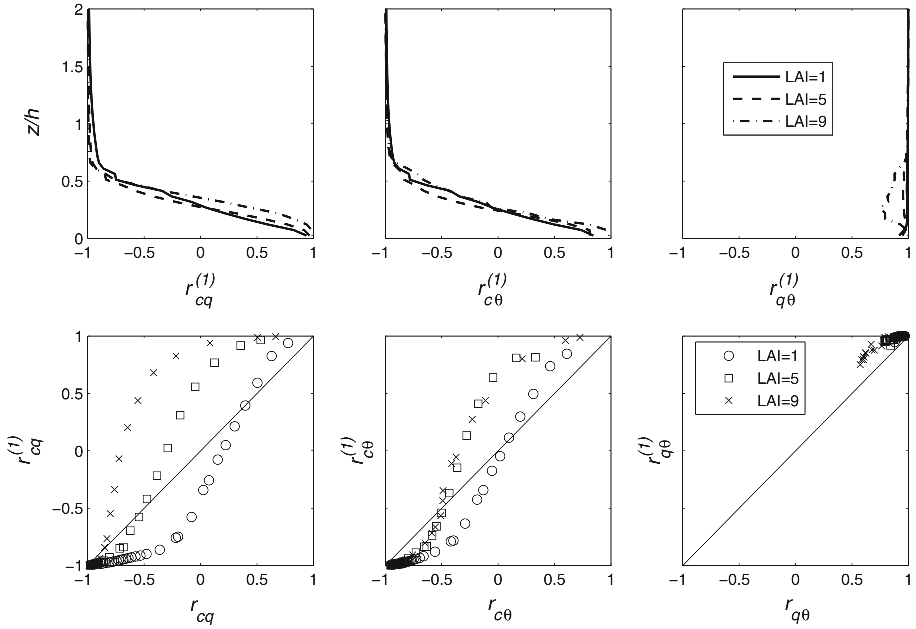

Fig. 14 (*Top row*) Vertical profiles of correlation coefficients of the 3D coherent structure among three scalars: $r_{cq}^{(1)}$, $r_{c\theta}^{(1)}$ and $r_{q\theta}^{(1)}$ from *left to right*; (*bottom row*) scatter plots between the correlation coefficients of the coherent structures and the corresponding counterparts obtained from the original field: $r_{cq}^{(1)}$, $r_{c\theta}^{(1)}$ and $r_{q\theta}^{(1)}$ from *left to right*

Fig. 8 that the incoherent components remaining in the original field after the extraction of the coherent structure are generally uncorrelated or weakly correlated, thus 'contaminating' the correlation in the original field and leading to $\left|r_{s_1 s_2}\right| < \left|r_{s_1 s_2}^{(1)}\right|$ for $\left|r_{s_1 s_2}\right| \gg 0$.

In Fig. 15, the result of ΔS_0 calculated for the truncated reconstruction $\mathrm{V}_i^{(1)}(x, y, z, t)$ with only the coherent structure, denoted as $\Delta S_0^{(1)}$, are presented. A comparison between $\Delta S_0^{(1)}$ and ΔS_0 then quantifies the skill of the coherent structure in approximating the sweep-ejection cycle in the original field. It appears that $\mathrm{V}_i^{(1)}(x, y, z, t)$ significantly increases the vertical range of ejection dominance from that of its original field evidenced by positive $\Delta S_0^{(1)}$ in the region of examination (cf. Fig. 6), although it also weakens the ejection dominance in the upper CSL. Note that this does not contradict the agreement with previous CSL results depicted in Figs. 10 and 11, which is mainly concerning the topology and the direction of the velocity components of the coherent structures (i.e. the sign of u_i') was forced (see e.g. [19,34]). This finding may not be entirely surprising. After all, some of the key dynamical features of the coherent structures are influenced by σ_u^2, which is primarily produced well above the canopy. Moreover, ΔS_0 is a function of triple moments (see Eq. (12) in [9]), which the POD identification strategy does not intend to preserve. Deep into the canopy, velocity variances decrease such that the POD becomes insensitive to any significant flow characteristics including the relative importance between sweeps and ejections in this region. The dependence on height is significantly weakened in $\Delta S_0^{(1)}$ when compared to that in ΔS_0 ,

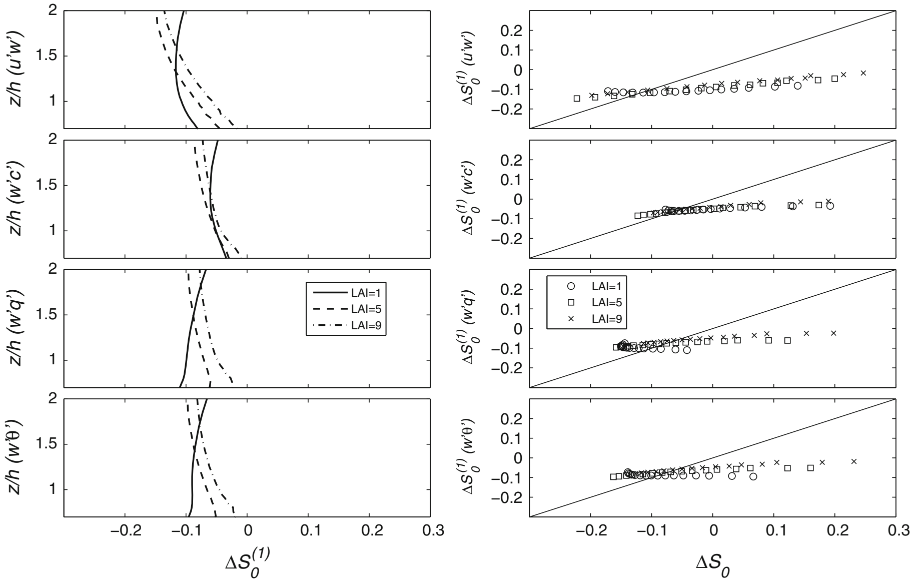

Fig. 15 (*Left column*) $\Delta S_0^{(1)}$ for $u'w'$, $w'c'$, $w'q'$ and $w'\theta'$ (from *top to bottom*); (*right column*) *scatter plots* between ΔS_0 and $\Delta S_0^{(1)}$ for $u'w'$, $w'c'$, $w'q'$ and $w'\theta'$ (from *top to bottom*)

as evidenced by the large deviations in the $\Delta S_0 - \Delta S_0^{(1)}$ scatter plot. The addition of one more eigenmode superposed, the truncated reconstruction $V_i^{(2)}(x, y, z, t)$ can perform much better than $V_i^{(1)}(x, y, z, t)$ in approximating the sweep-ejection cycle in the original field. $\Delta S_0^{(2)}$ contains a vertical range of ejection dominance closer to ΔS_0 and presents more dependence on height than does $\Delta S_0^{(1)}$ (not shown here). To reveal the effects of higher order modes on the sweep-ejection cycle, we present the trend of $\Delta S_0^{(n)}$ approaching ΔS_0 with $n = 1, 2, 5$ and 10 respectively, using the case of $LAI = 5$ in Fig. 16. While it is expected that the inclusion of higher order modes will enhance the approximation of $\Delta S_0^{(n)}$ to ΔS_0 , it is found that only five modes (with about 75 % of total variances retained as indicated in Fig. 7) are able to closely capture the values of ΔS_0 above the canopy and the sign and trend of ΔS_0 inside the canopy. For sweeps $\Delta S_0^{(n)}$ approaches ΔS_0 with a generally better performance for momentum than for the scalars due to the reason mentioned above regarding velocity variances.

4 Conclusions

The dissimilarity of turbulent transport between two scalars within the CSL has mainly been attributed to differences in the distribution of scalar sources and sinks throughout the canopy. Since the large-scale coherent structures carry the information of the vertical distribution of the scalar sources and sinks, we hypothesize that their morphological features significantly affect the resulting scalar dissimilarity. This study tests this hypothesis by simulating the interaction between canopy, turbulent transport and biophysical mechanisms over a forest of horizontally homogeneous foliage density where LAI ranged from sparse (= 1) to dense

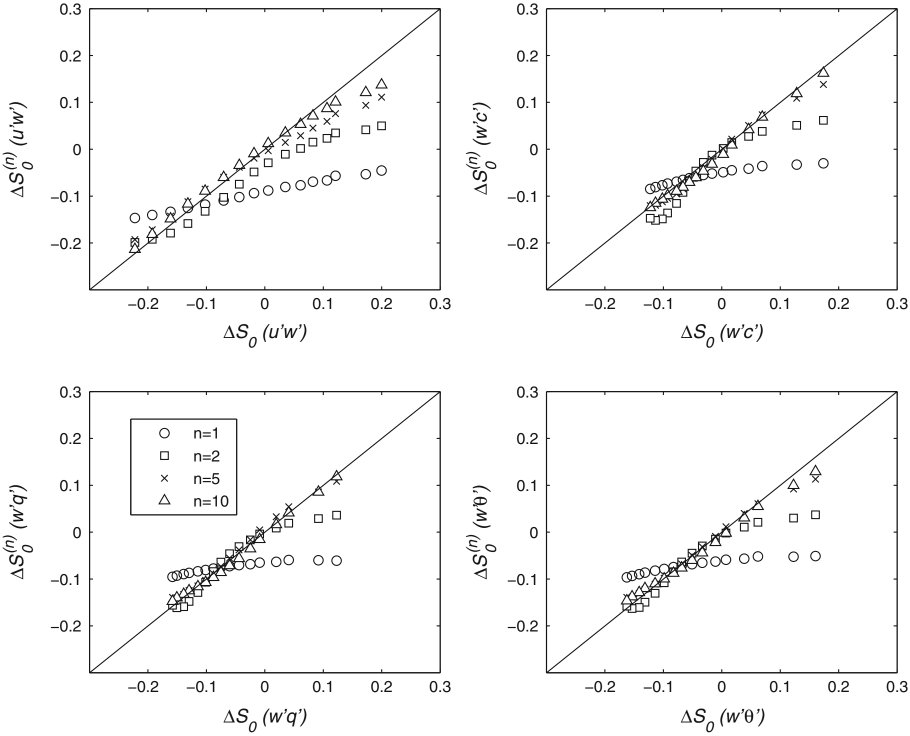

Fig. 16 *Scatter plots* between ΔS_0 and $\Delta S_0^{(n)}$ ($n = 1, 2, 5$ and 10) for $u'w'$, $w'c'$, $w'q'$ and $w'\theta'$, respectively. Note that only resolved velocity and scalar quantities are used to produce this result

(= 9). The simulations were performed under prevailing environmental conditions of a single mid-day period with high sun angles and a prescribed saturation of soil moisture. The coherent structure is educed through the use of the proper orthogonal decomposition and the shot-effect expansion. Two approaches were mainly used in the formulation of the POD: one based on velocity variances and another based on the joint velocity and scalar variances. The two approaches yielded similar results in terms of their geometric features of the velocity components. Based on the LES results and POD analysis, we found the following about the scalar–scalar dissimilarity and the role of the coherent structure:

1. A significant negative correlation between c and q from the top of the CSL down to a certain height ($z/h \approx 0.3$) within the canopy exists and this correlation is enhanced as the canopy becomes denser since the CO_2 sink and the water vapour source become both stomatally regulated. Near the ground surface, c and q exhibit a positive correlation owing to that the ground surface emits CO_2 produced by litter and soil respiration and also water vapour through soil (and litter) evaporation. In the middle canopy, c and q are rather uncorrelated or weakly correlated. The CO_2 source from the ground appears to increase its turbulent Schmidt number when compared to the other scalars. On the contrary, the water vapour source and the sensible heat source tend to decrease their corresponding turbulent Schmidt number. In addition to the impact on turbulent Schmidt number, the water vapour source and the heat source at the ground level also influence their corresponding sweep-ejection cycle by enhancing the relative importance of ejection.

2. Coherent structure approximates the turbulent Schmidt numbers obtained from the original LES fields. A basic agreement is also found in scalar–scalar correlation coefficients between the coherent structure and the original field with the coherent structure tending to magnify the magnitude of the scalar–scalar correlation when this correlation is strong. Finally, the ability of the coherent structure to describe the sweep-ejection cycle of the original field is also investigated. It was found that the first mode poorly represents the relative importance of sweep/ejection in the original field with the discrepancy mainly appearing as the lack of the sweep dominance inside the canopy. However, the superposition of higher order modes on the leading mode largely diminishes this discrepancy. Moreover, the convergence here is rather rapid with five modes recovering much of the ejection-sweep properties inside and above the canopy. This is the first such result concerning sweep/ejection events of scalars.

The broader impacts of this work are three fold: On the measurement side, there is now interest in partitioning eddy-covariance fluxes of CO_2 and water vapour into foliage versus forest floor using precisely the scalar dissimilarity [63,74]. We showed here that the success of such approaches depends on the spatial coherency of the organized structure. On the modelling side, we showed that the similarity in Schmidt numbers among scalars, used virtually in all footprint models, may not be valid and does depend on how coupled the coherent structure is to the forest floor. Finally, from a theoretical perspective, this work illustrates the potential for using lower-dimensional models for scalar exchange across the vegetation–atmosphere interface.

Acknowledgments Huang and Albertson acknowledge the support provided by the Department of Energy Southeastern Regional Center of the National Institute for Climate Change Research (Grant # DE-FC02-06ER64156), and by the United States Department of Agriculture (Grant # 58-1265-5-046-02). Katul acknowledges support from the U.S. Department of Energy through the Office of Biological and Environmental Research (BER) Terrestrial Carbon Processes (TCP) program (DE-SC000697), the National Science Foundation (NSF-AGS-1102227, NSF-EAR-10-13339, and NSF-CBET-103347), the U.S. Department of Agriculture (2011-67003-30222), and the Binational Agricultural Research and Development (BARD) fund (IS-4374-11C).

Appendix 1: A general POD approach in the wavenumber space

For continuous applications, Eq. (9) has a countable infinity of solutions [27], each including an eigenvalue $\lambda^{(n)}$ and an associated eigenfunction $\hat{\phi}_i^{(n)}$, where the index n is added to distinguish between different solutions. However, for the application of this paper, the approach of discretization needs to be conducted such that the solutions are finite (see e.g. [70]). For convenience, we maintain the notation of continuous conditions. The eigenfunctions are orthogonal and can be normalized such that

$$\int_H \hat{\phi}_i^{(m)}(k_x, k_y, z)\hat{\phi}_i^{(n)*}(k_x, k_y, z)\mathrm{d}z = \delta_{mn}. \tag{17}$$

We may sort the series of solutions by decreasing magnitude of the modulus of $\lambda^{(n)}$ such that $\lambda^{(1)} > \lambda^{(2)} > \cdots$, and define eigenmode as $\hat{\psi}_i^{(n)} = \sqrt{\lambda^{(n)}}\hat{\phi}_i^{(n)}$ such that $\hat{\psi}_i^{(n)}$ carry the information of both the spatial shape and its importance toward describing the variance [19].

The POD of $\hat{\mathrm{V}}$ can now be expressed based on the eigenfunctions,

$$\hat{\mathrm{V}}_i(k_x, k_y, z, t) = \sum_{n=1}^{\infty} \hat{a}^{(n)}(k_x, k_y, t)\hat{\phi}_i^{(n)}(k_x, k_y, z), \tag{18}$$

where $\hat{a}^{(n)}$ is the coefficient corresponding to $\hat{\phi}_i^{(n)}$. Multiply both sides of Eq. (18) by $\hat{\phi}_i^{(m)*}$, integrate in z over H and then substitute Eq. (17) into the resulting equation, we obtain the expression of the coefficient $\hat{a}^{(n)}$ as

$$\hat{a}^{(n)}(k_x, k_y, t) = \int_H \hat{\mathrm{V}}_i(k_x, k_y, z, t)\hat{\phi}_i^{(n)*}(k_x, k_y, z)\mathrm{d}z. \tag{19}$$

$\hat{a}^{(n)}$ is also orthogonal across different solutions in the sense that

$$\langle \hat{a}^{(m)}(k_x, k_y, t)\hat{a}^{(n)*}(k_x, k_y, t)\rangle_t = \delta_{mn}\lambda(k_x, k_y). \tag{20}$$

Combining Eq. (10) and Eq. (18), we can obtain the reconstruction formula of Φ_{ij} from $\hat{\phi}_i^{(n)}$ as

$$\Phi_{ij}(k_x, k_y, z, \tilde{z}) = \sum_{n=1}^{\infty} \lambda^{(n)}(k_x, k_y)\hat{\phi}_i^{(n)}(k_x, k_y, z)\hat{\phi}_j^{(n)*}(k_x, k_y, \tilde{z}). \tag{21}$$

The two-point correlation tensor is the inverse Fourier transform of Eq. (21)

$$R_{ij}(r_x, r_y, z, \tilde{z}) = \frac{1}{4\pi^2}\sum_{n=1}^{\infty}\iint \lambda^{(n)}(k_x, k_y)\hat{\phi}_i^{(n)}(k_x, k_y, z)\hat{\phi}_j^{(n)*}(k_x, k_y, \tilde{z})e^{ik_x r_x + ik_y r_y}\mathrm{d}k_x\mathrm{d}k_y, \tag{22}$$

where r_x and r_y are separation distances in x and y, respectively. Letting $r_x = r_y = 0$ and $z = \tilde{z}$ leads to the one-point second-order statistics

$$\langle \mathrm{V}_i\mathrm{V}_j\rangle(z) = \frac{1}{4\pi^2}\sum_{n=1}^{\infty}\iint \lambda^{(n)}(k_x, k_y)\hat{\phi}_i^{(n)}(k_x, k_y, z)\hat{\phi}_j^{(n)*}(k_x, k_y, z)e^{ik_x r_x + ik_y r_y}\mathrm{d}k_x\mathrm{d}k_y. \tag{23}$$

Furthermore, letting $i = j$ and integrating z over H, the conservation of the overall variance is given by

$$E = \int_H \langle \mathrm{V}_i\mathrm{V}_i\rangle(z)\mathrm{d}z = \frac{1}{4\pi^2}\sum_{n=1}^{\infty}\iint \lambda^{(n)}(k_x, k_y)\mathrm{d}k_x\mathrm{d}k_y. \tag{24}$$

If we write $\Lambda^{(n)} = \frac{1}{4\pi^2}\sum_{n=1}^{\infty}\iint \lambda^{(n)}(k_x, k_y)\mathrm{d}k_x\mathrm{d}k_y$, then

$$E = \sum_{n=1}^{\infty} \Lambda^{(n)}. \tag{25}$$

The original field of V_i can be approximated by a truncated reconstruction using the first p eigenvalue/eigenfunction solutions [conf. Eq. (18)]:

$$\mathrm{V}_i^{(p)}(x, y, z, t) = \frac{1}{4\pi^2}\sum_{n=1}^{p}\iint \hat{a}^{(n)}(k_x, k_y, t)\hat{\phi}_i^{(n)}(k_x, k_y, z)e^{ik_x r_x + ik_y r_y}\mathrm{d}k_x\mathrm{d}k_y, \tag{26}$$

and the contribution of $V_i^{(p)}$ to the second-order statistics is given by,

$$\langle V_i^{(p)} V_j^{(p)} \rangle (z) = \frac{1}{4\pi^2} \sum_{n=1}^{p} \iint \lambda^{(n)}(k_x, k_y) \hat{\phi}_i^{(n)}(k_x, k_y, z) \hat{\phi}_j^{(n)*}(k_x, k_y, z) e^{ik_x r_x + ik_y r_y} \mathrm{d}k_x \mathrm{d}k_y. \tag{27}$$

The 3D coherent structure has been referred to here as the first eigenmode $\psi_i^{(1)}$ since $\Lambda^{(1)}$ represents the greatest percentage of E out of all other non-Fourier-mode choices of the coherent structure [19,27,33,34,53]. However, the POD framework does not provide the phase angles for $\phi_i^{(1)}$, which are critical in determining the spatial shape of the coherent structure in the physical space. This issue is commonly tackled through the shot-effect expansion theory [50] in conjunction with an extra assumption regarding the physical property of the coherent structure. For example, Lumley [50] proposed the bi-spectrum or three-point correlation criterion, which states that the coherent structure should conserve as much as possible the three-point correlation of the original velocity field. The second method, termed the 'compactness criterion', was originally proposed by [26], and assumes that the coherent structure is spatially compact. The third method is termed the 'wavenumber continuity' or the 'spectral smoothness' criterion, which implies that the phase angle of the coherent structure is continuous in wavenumber space [53]. In this paper, we apply the compactness criterion considering that the coherent structures in the CSL revealed by flow visualization experiments are typically compact [55]. Finnigan et al. [20] compared the coherent structures derived from the POD together with the compactness criterion and from a conditional average method using local maxima of static pressure at the canopy top as a trigger, and found that unlike the latter, the former does not reveal that a sweep motion is often followed by an ejection motion downstream. However, this does not affect our use of the POD approach as far as the topic of this paper is concerned because scalar dissimilarity is dominant in the vertical direction. Additionally, the orientation of the coherent structure is forced to be consistent with a sweep motion owing to the known fact that sweep is the dominant contributor to the Reynolds stress within the canopy [19]. Denoting the phase angles as $\eta(k_x, k_y)$, the coherent structure can now be written as

$$\psi_i^{(1)}(r_x, r_y, z) = \frac{1}{4\pi^2} \iint \sqrt{\lambda^{(1)}(k_x, k_y)} \hat{\phi}_i^{(1)}(k_x, k_y, z) e^{ik_x r_x + ik_y r_y + i\eta(k_x, k_y)} \mathrm{d}k_x \mathrm{d}k_y. \tag{28}$$

$\psi_i^{(1)}$ connects to $V_i^{(1)}$ by

$$V_i^{(1)}(x, y, z, t) = \iint \psi_i^{(1)}(x - \tilde{x}, y - \tilde{y}, z) \beta(\tilde{x}, \tilde{y}, t) \mathrm{d}\tilde{x} \mathrm{d}\tilde{y}, \tag{29}$$

where

$$\beta(x, y, t) = \frac{1}{4\pi^2} \iint \hat{a}^{(1)}(k_x, k_y, t) e^{-i\eta k_x, k_y} \Big/ \sqrt{\lambda^{(1)}(k_x, k_y)} \mathrm{d}k_x \mathrm{d}k_y, \tag{30}$$

and $\beta(x, y, t)$ satisfies

$$\langle \beta(x, y, t) \beta(\tilde{x}, \tilde{y}, t) \rangle_t = \delta(x - \tilde{x}, y - \tilde{y}). \tag{31}$$

The variance $\Lambda^{(1)}$ is conserved in $V_i^{(1)}$ as well as in $\psi_i^{(1)}$, given by

$$\iiint \langle V_i^{(1)}(x, y, z, t)^2 \rangle_t \mathrm{d}x \mathrm{d}y \mathrm{d}z = \iiint \psi_i^{(1)}(r_x, r_y, z)^2 \mathrm{d}r_x \mathrm{d}r_y \mathrm{d}z = \Lambda^{(1)}. \tag{32}$$

References

1. Albertson JD, Parlange MB (1999a) Natural integration of scalar fluxes from complex terrain. Adv Water Resour 23(3):239–252. doi:10.1016/S0309-1708(99)00011-1
2. Albertson JD, Parlange MB (1999b) Surface length scales and shear stress: implications for land–atmosphere interaction over complex terrain. Water Resour Res 35(7):2121–2132. doi:10.1029/1999WR900094
3. Albertson JD, Parlange M, Katul G, Chu CR, Stricker H (1995) Sensible heat-flux from arid regions—a simple flux-variance method. Water Resour Res 31(4):969–973. doi:10.1029/94WR02978
4. Albertson JD, Katul GG, Wiberg P (2001) Relative importance of local and regional controls on coupled water, carbon, and energy fluxes. Adv Water Resour 24(9–10):1103–1118. doi:10.1016/S0309-1708(01)00042-2
5. Berkooz G, Holmes P, Lumley JL (1993) The proper orthogonal decomposition in the analysis of turbulent flows. Annu Rev Fluid Mech 25:539–575. doi:10.1146/annurev.fluid.25.1.539
6. Brunet Y, Finnigan JJ, Raupach MR (1994) A wind-tunnel study of air-flow in waving wheat—single-point velocity statistics. Boundary-Layer Meteorol 70(1–2):95–132. doi:10.1007/BF00712525
7. Campbell GS, Norman JM (1998) An introduction to environmental biophysics. Springer, New York
8. Cassiani M, Katul GG, Albertson JD (2008) The effects of canopy leaf area index on airflow across forest edges: large-eddy simulation and analytical results. Boundary-Layer Meteorol 126(3):433–460. doi:10.1007/s10546-007-9242-1
9. Cava D, Katul GG, Scrimieri A, Poggi D, Cescatti A, Giostra U (2006) Buoyancy and the sensible heat flux budget within dense canopies. Boundary-Layer Meteorol 118(1):217–240. doi:10.1007/s10546-005-4736-1
10. Cava D, Katul GG, Sempreviva AM, Giostra U, Scrimieri A (2008) On the anomalous behaviour of scalar flux-variance similarity functions within the canopy sub-layer of a dense alpine forest. Boundary-Layer Meteorol 128(1):33–57. doi:10.1007/s10546-008-9276-z
11. Cescatti A, Marcolla B (2004) Drag coefficient and turbulence intensity in conifer canopies. Agric For Meteorol 121(3–4):197–206. doi:10.1016/j.agrformet.2003.08.028
12. De Bruin HAR, Van Den Hurk BJJM, Kroon LJM (1999) On the temperature–humidity correlation and similarity. Boundary-Layer Meteorol 93(3):453–468. doi:10.1023/A:1002071607796
13. Dupont S, Brunet Y (2009) Coherent structures in canopy edge flow: a large-eddy simulation study. J Fluid Mech 630:93–128. doi:10.1017/S0022112009006739
14. Dupont S, Patton EG (2012) Momentum and scalar transport within a vegetation canopy following atmospheric stability and seasonal canopy changes: the chats experiment. Atmos Chem Phys Discuss 12:6363–6418. doi:10.5194/acpd-12-6363-2012
15. Dupont S, Gosselin F, Py C, de langre E, Hemon P, Brunet Y (2010) Modelling waving crops using large-eddy simulation: comparison with experiments and a linear stability analysis. J Fluid Mech 652:5–44. doi:10.1017/S0022112010000686
16. Dupont S, Irvine MR, Bonnefond JM, Lamaud E, Brunet Y (2012) Turbulent structures in a pine forest with a deep and sparse trunk space: Stand and edge regions. Boundary-Layer Meteorol 143(2):309–336. doi:10.1007/s10546-012-9695-8
17. Ellsworth DS, Oren R, Huang C, Phillips N, Hendrey GR (1995) Leaf and canopy responses to elevated CO_2 in a pine forest under free-air CO_2 enrichment. Oecologia 104(2):139–146. doi:10.1007/BF00328578
18. Farquhar G, von Caemmerer S, Berry JA (1980) A biochemical model of photosynthetic CO_2 assimilation in leaves of C_3 species. Planta 149:78–90
19. Finnigan JJ, Shaw RH (2000) A wind-tunnel study of airflow in waving wheat: an EOF analysis of the structure of the large-eddy motion. Boundary-Layer Meteorol 96(1–2):211–255. doi:10.1023/A:1002618621171
20. Finnigan JJ, Shaw RH, Patton EG (2009) Turbulence structure above a vegetation canopy. J Fluid Mech 637:387–424. doi:10.1017/S0022112009990589
21. Flesch TK, Prueger JH, Hatfield JL (2002) Turbulent Schmidt number from a tracer experiment. Agric For Meteorol 111(4):299–307. doi:10.1016/S0168-1923(02)00025-4
22. Gao W, Shaw RH, Paw KT (1989) Observation of organized structure in turbulent-flow within and above a forest canopy. Boundary-Layer Meteorol 47(1–4):349–377. doi:10.1007/BF00122339
23. Garratt JR (1992) The atmospheric boundary layer. Cambridge University Press, Cambridge
24. Guo X, Zhang H, Cai X, Kang L, Zhu T, Leclerc MY (2009) Flux-variance method for latent heat and carbon dioxide fluxes in unstable conditions. Boundary-Layer Meteorol 131(3):363–384. doi:10.1007/s10546-009-9377-3

25. Harman IN, Finnigan JJ (2008) Scalar concentration profiles in the canopy and roughness sublayer. Boundary-Layer Meteorol 129(3):323–351. doi:10.1007/s10546-008-9328-4
26. Herzog S (1986) The large scale structure in the near-wall region of turbulent pipe flow. PhD thesis, Cornell University
27. Holmes P, Lumley JL, Berkooz G (1996) Turbulence, coherent structures, dynamical systems, and symmetry. Cambridge University Press, New York
28. Horst TW, Weil JC (1992) Footprint estimation for scalar flux measurements in the atmospheric surface-layer. Boundary-Layer Meteorol 59(3):279–296. doi:10.1007/BF00119817
29. Hsieh CI, Katul G (2009) The lagrangian stochastic model for estimating footprint and water vapor fluxes over inhomogeneous surfaces. Int J Biometeorol 53(1):87–100. doi:10.1007/s00484-008-0193-0
30. Hsieh CI, Katul GG, Schieldge J, Sigmon J, Knoerr KR (1996) Estimation of momentum and heat fluxes using dissipation and flux-variance methods in the unstable surface layer. Water Resour Res 32(8):2453–2462. doi:10.1029/96WR01337
31. Hsieh CI, Lai MC, Hsia YJ, Chang TJ (2008) Estimation of sensible heat, water vapor, and CO(2) fluxes using the flux-variance method. Int J Biometeorol 52(6):521–533. doi:10.1007/s00484-008-0149-4
32. Huang J, Bou-Zeid E (2013) Turbulence and vertical fluxes in the stable atmospheric boundary-layer I: a large-eddy simulation study. J Atmos Sci. doi:10.1175/JAS-D-12-0167.1
33. Huang J, Cassiani M, Albertson JD (2009a) Analysis of coherent structures within the atmospheric boundary layer. Boundary-Layer Meteorol 131(2):147–171. doi:10.1007/s10546-009-9357-7
34. Huang J, Cassiani M, Albertson JD (2009b) The effects of vegetation density on coherent turbulent structures within the canopy sublayer: a large-eddy simulation study. Boundary-Layer Meteorol 133(2):253–275. doi:10.1007/s10546-009-9423-1
35. Huang J, Cassiani M, Albertson JD (2011) Coherent turbulent structures across a vegetation discontinuity. Boundary-Layer Meteorol 140(1):1–22. doi:10.1007/s10546-011-9600-x
36. Kaimal JC, Finnigan JJ (1994) Atmospheric boundary layer flows: their structure and measurement. Oxford University Press, New York
37. Katul G, Goltz SM, Hsieh CI, Cheng Y, Mowry F, Sigmon J (1995) Estimation of surface heat and momentum fluxes using the flux-variance method above uniform and nonuniform terrain. Boundary-Layer Meteorol 74(3):237–260. doi:10.1007/BF00712120
38. Katul G, Hsieh CI, Oren R, Ellsworth D, Phillips N (1996) Latent and sensible heat flux predictions from a uniform pine forest using surface renewal and flux variance methods. Boundary-Layer Meteorol 80(3):249–282
39. Katul GG, Albertson JD (1998) An investigation of higher-order closure models for a forested canopy. Boundary-Layer Meteorol 89(1):47–74. doi:10.1023/A:1001509106381
40. Katul GG, Chang WH (1999) Principal length scales in second-order closure models for canopy turbulence. J Appl Meteorol 38(11):1631–1643. doi:10.1175/1520-0450(1999)038<1631:PLSISO>2.0.CO;2
41. Katul GG, Sempreviva AM, Cava D (2008) The temperature–humidity covariance in the marine surface layer: a one-dimensional analytical model. Boundary-Layer Meteorol 126(2):263–278. doi:10.1007/s10546-007-9236-z
42. Katul GG, Cava D, Launiainen S, Vesala T (2009) An analytical model for the two-scalar covariance budget inside a uniform dense canopy. Boundary-Layer Meteorol 131(2):173–192. doi:10.1007/s10546-009-9361-y
43. Koeltzsch K (2000) The height dependence of the turbulent Schmidt number within the boundary layer. Atmos Environ 34(7):1147–1151. doi:10.1016/S1352-2310(99)00369-6
44. Kosovic B (1997) Subgrid-scale modelling for the large-eddy simulation of high-Reynolds-number boundary layers. J Fluid Mech 336:151–182. doi:10.1017/S0022112096004697
45. Lamaud E, Irvine M (2006) Temperature-humidity dissimilarity and heat-to-water-vapour transport efficiency above and within a pine forest canopy: the role of the Bowen ratio. Boundary-Layer Meteorol 120(1):87–109. doi:10.1007/s10546-005-9032-6
46. Leclerc MY, Thurtell GW (1990) Footprint prediction of scalar fluxes using a markovian analysis. Boundary-Layer Meteorol 52(3):247–258. doi:10.1007/BF00122089
47. Li D, Bou-Zeid E (2011) Coherent structures and the dissimilarity of turbulent transport of momentum and scalars in the unstable atmospheric surface layer. Boundary-Layer Meteorol 140:243–262. doi:10.1007/s10546-011-9613-5
48. Lumley JL (1967) The structure of inhomogeneous turbulent flows. In: Yagolm AM, Tatarsky VI (eds) Atmospheric turbulence and radio wave propagation. Nauka, Moscow, pp 166–178
49. Lumley JL (1970) Stochastic tools in turbulence. Academic Press, New York
50. Lumley JL (1981) Coherent structures in turbulence. In: Meyer RE (ed) Transition and turbulence. Academic Press, New York, pp 215–241

51. Mason PJ, Thomson DJ (1992) Stochastic backscatter in large-eddy simulations of boundary-layers. J Fluid Mech 242:51–78. doi:10.1017/S0022112092002271
52. Moeng CH (1984) A large-eddy-simulation model for the study of planetary boundary-layer turbulence. J Atmos Sci 41(13):2052–2062. doi:10.1175/1520-0469(1984)041<2052:ALESMF>2.0.CO;2
53. Moin P, Moser RD (1989) Characteristic-eddy decomposition of turbulence in a channel. J Fluid Mech 200:471–509. doi:10.1017/S0022112089000741
54. Poggi D, Katul GG, Albertson JD (2004a) Momentum transfer and turbulent kinetic energy budgets within a dense model canopy. Boundary-Layer Meteorol 111(3):589–614. doi:10.1023/B:BOUN.0000016502.52590.af
55. Poggi D, Porporato A, Ridolfi L, Albertson JD, Katul GG (2004b) The effect of vegetation density on canopy sub-layer turbulence. Boundary-Layer Meteorol 111(3):565–587. doi:10.1023/B:BOUN.0000016576.05621.73
56. Porté-Agel F, Meneveau C, Parlange MB (2000) A scale-dependent dynamic model for large-eddy simulation: application to a neutral atmospheric boundary layer. J Fluid Mech 415:261–284
57. Porté-Agel F, Wu YT, Lu H, Conzemius RJ (2011) Large-eddy simulation of atmospheric boundary layer flow through wind turbines and wind farms. J Wind Eng Ind Aerodyn 99(4):154–168. doi:10.1016/j.jweia.2011.01.011
58. Raupach MR (1981) Conditional statistics of reynolds stress in rough-wall and smooth-wall turbulent boundary-layers. J Fluid Mech 108(Jul):363–382. doi:10.1017/S0022112081002164
59. Raupach MR (1988) Canopy transport processes. In: Steffen WL, Denmead OT (eds) Flow and transport in the natural environment: advances and applications. Springer, Berlin, pp 95–127
60. Raupach MR, Thom AS (1981) Turbulence in and above plant canopies. Annu Rev Fluid Mech 13:97–129. doi:10.1146/annurev.fl.13.010181.000525
61. Raupach MR, Finnigan JJ, Brunet Y (1996) Coherent eddies and turbulence in vegetation canopies: the mixing-layer analogy. Boundary-Layer Meteorol 78:351–382
62. Scanlon TM, Albertson JD (2001) Turbulent transport of carbon dioxide and water vapor within a vegetation canopy during unstable conditions: identification of episodes using wavelet analysis. J Geophys Res 106(D7):7251–7262. doi:10.1029/2000JD900662
63. Scanlon TM, Kustas WP (2010) Partitioning carbon dioxide and water vapor fluxes using correlation analysis. Agric For Meteorol 150(1):89–99. doi:10.1016/j.agrformet.2009.09.005
64. Scanlon TM, Sahu P (2008) On the correlation structure of water vapor and carbon dioxide in the atmospheric surface layer: a basis for flux partitioning. Water Resour Res 44(10):W10418. doi:10.1029/2008WR006932
65. Schmidt H, Schumann U (1989) Coherent structure of the convective boundary-layer derived from large-eddy simulations. J Fluid Mech 200:511–562. doi:10.1017/S0022112089000753
66. Shaw RH, Schumann U (1992) Large-eddy simulation of turbulent-flow above and within a forest. Boundary-Layer Meteorol 61(1–2):47–64. doi:10.1007/BF02033994
67. Sirovich L (1987a) Turbulence and the dynamics of coherent structures. 1. Coherent structures. Q Appl Math 45(3):561–571
68. Sirovich L (1987b) Turbulence and the dynamics of coherent structures. 2. Symmetries and transformations. Q Appl Math 45(3):573–582
69. Sirovich L (1987c) Turbulence and the dynamics of coherent structures. 3. Dynamics and scaling. Q Appl Math 45(3):583–590
70. Smith TR, Moehlis J, Holmes P (2005) Low-dimensional modelling of turbulence using the proper orthogonal decomposition: a tutorial. Nonlinear Dyn 41(1–3):275–307. doi:10.1007/s11071-005-2823-y
71. Stull RB (1988) An introduction to boundary layer meteorology. Kluwer, Dordrecht
72. Sullivan PP, McWilliams JC, Moeng CH (1996) A grid nesting method for large-eddy simulation of planetary boundary-layer flows. Boundary-Layer Meteorol 80(1–2):167–202. doi:10.1007/BF00119016
73. Thomas C, Foken T (2007) Flux contribution of coherent structures and its implications for the exchange of energy and matter in a tall spruce canopy. Boundary-Layer Meteorol 123(2):317–337. doi:10.1007/s10546-006-9144-7
74. Thomas C, Martin JG, Goeckede M, Siqueira MB, Foken T, Law BE, Loescher HW, Katul G (2008) Estimating daytime subcanopy respiration from conditional sampling methods applied to mufti-scalar high frequency turbulence time series. Agric For Meteorol 148(8–9):1210–1229. doi:10.1016/j.agrformet.2008.03.002
75. Vesala T, Kljun N, Rannik U, Rinne J, Sogachev A, Markkanen T, Sabelfeld K, Foken T, Leclerc MY (2008) Flux and concentration footprint modelling: state of the art. Environ Pollut 152(3):653–666. doi:10.1016/j.envpol.2007.06.070
76. Williams CA, Scanlon TM, Albertson JD (2007) Influence of surface heterogeneity on scalar dissimilarity in the roughness sublayer. Boundary-Layer Meteorol 122(1):149–165. doi:10.1007/s10546-006-9097-x

77. Wilson NR, Shaw RH (1977) Higher-order closure model for canopy flow. J Appl Meteorol 16(11):1197–1205. doi:10.1175/1520-0450(1977)016<1197:AHOCMF>2.0.CO;2
78. Yang B, Morse AP, Shaw RH, Paw U KT (2006a) Large-eddy simulation of turbulent flow across a forest edge. Part II: momentum and turbulent kinetic energy budgets. Boundary-Layer Meteorol 121(3):433–457. doi:10.1007/s10546-006-9083-3
79. Yang B, Raupach MR, Shaw RH, Tha K, Paw U KT, Morse AP (2006b) Large-eddy simulation of turbulent flow across a forest edge. Part I: flow statistics. Boundary-Layer Meteorol 120(3):377–412. doi:10.1007/s10546-006-9057-5